Nonlinear transport current flow in superconductors with planar obstacles

Alex Gurevich and Mark Friesen
Applied Superconductivity Center, University of Wisconsin, Madison, Wisconsin 53706
(Received 13 January 2000)

We present a detailed description of a hodograph method, which enables us to calculate analytically the two-dimensional distributions of the electric field $\mathbf{E}(\mathbf{r})$ and transport current density $\mathbf{J}(\mathbf{r})$ in superconductors, taking into account their highly nonlinear E-J characteristics. The method gives a unique solution $\mathbf{E}(\mathbf{r})$ of nonlinear steady-state Maxwell's equations for given boundary conditions, showing applicability limits of the critical state model and pointing out where it breaks down. The nonlinear problem of calculation of $\mathbf{J}(\mathbf{r})$ by the hodograph method reduces to solving a *linear* equation for the electric potential $\varphi(\mathbf{E})$, or the current stream function $\psi(\mathbf{E})$ as a function of $\mathbf{E}$. For the power-law characteristics $E=E_c(J/J_c)^n$, calculation of $\mathbf{E}(\mathbf{r})$ and $\mathbf{J}(\mathbf{r})$ can be mapped onto solutions of the London equation with the inverse screening length $\beta=(n-1)/2\sqrt{n}$ in the hodograph space (E_xE_y). We give general methods of solving the hodograph equations and obtain closed-form analytical solutions for particular current flows. The method is applied to calculate distributions of $\mathbf{E}(\mathbf{r})$ and dissipation in superconductors with macroscopic planar defects, such as high-angle grain boundaries, microcracks, etc. Current patterns around planar obstacles are shown to break up into domains of different orientations of $\mathbf{J}$, separated by current domain walls. We calculate the structure of the current domain walls, whose width depends both on the geometry of current flow and the exponent n. These domain walls differ from the current discontinuity lines of the Bean model even in the limit $n\to\infty$. We obtained a solution for current flow past a planar defect of length $2a$ in an infinite superconductor and showed that the defect causes strong local electric-field enhancement and long-range disturbances of $\mathbf{E}(\mathbf{r})$ on length scales $L_\perp\sim an \gg a$ and $L_\parallel\sim a\sqrt{n}\gg a$ perpendicular and parallel to the mean current flow, respectively. This solution also exhibits large stagnation regions of magnetic flux near planar defects, universal distributions of $\mathbf{J}(\mathbf{r})$ in the critical state limit, $n\to\infty$, and local flux flow regions near the edges. We calculate Joule heating for nonlinear current flow and show that planar defects cause significant excess dissipation, which affects ac losses and local thermal instabilities in superconductors.

I. INTRODUCTION

Macroscopic electrodynamics of type-II superconductors in the mixed state is determined by the pinning and thermally activated creep of vortex structures, which gives rise to a weakly dissipative critical current, irreversible magnetization, and slow current relaxation (flux creep). These phenomena manifest themselves on length scales much larger than the Larkin pinning correlation length L_c, on which the critical state is formed.[1] On these macroscopic scales $L\gg L_c$, the only material characteristic which determines the behavior of superconductors in electromagnetic fields is the nonlinear local relation between the electric field $\mathbf{E}$ and current density $\mathbf{J}$,

$$\mathbf{J}=\frac{\mathbf{E}}{E}J(E). \tag{1}$$

Here $\mathbf{E}(\mathbf{r},t)$ and $\mathbf{J}(\mathbf{r},t)$ refer to the macroscopic electric field and current density averaged over all relevant intrinsic scales of pinned vortex structure, such as intervortex spacing, pinning correlation lengths, etc. We consider an isotropic E-J relation (1), which, for example, models the nearly two-dimensional (2D) current flow in the ab plane of layered high-temperature superconductors (HTS's). Equation (1), combined with the Maxwell equations

$$\partial_t\mathbf{B}=-\nabla\times\mathbf{E},\quad \nabla\times\mathbf{H}=\mathbf{J}(\mathbf{E}), \tag{2}$$

enable one to calculate the evolution of nonuniform distributions of $\mathbf{E}(\mathbf{r},t)$ and $\mathbf{B}(\mathbf{r},t)$ and thus to describe macroscopic magnetic, transport, and relaxation phenomena in superconductors.[1–4]

A type-II superconductor in the mixed state exhibits a highly nonlinear $E(J)$ dependence below a critical current density J_c, which separates regimes of flux flow at $J>J_c$ and flux creep at $J<J_c$ (Fig. 1). The crucial behavior of $E(J)$ at $J<J_c$ is determined by thermally activated vortex creep:

$$E(J)=E_c\exp\left[-\frac{U(J,T,B)}{T}\right], \tag{3}$$

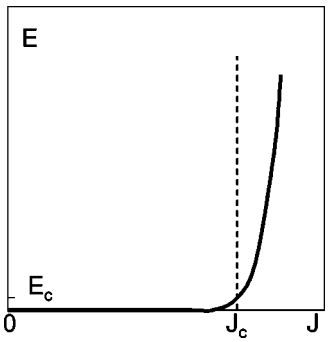

FIG. 1. E-J characteristic of a type-II superconductor.

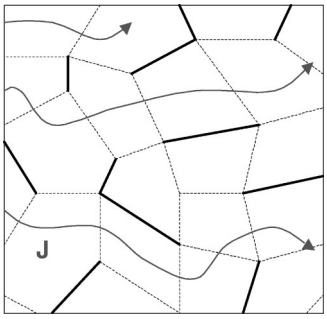

FIG. 2. Percolative current flow in polycrystals. Current-blocking high-angle grain boundaries are shown as solid lines, while low-angle grain boundaries, transparent to current flow, are shown as dashed lines.

where $U(J,T,B)$ is an activation barrier, which depends on J, the temperature T, and the magnetic induction, B. Here E_c is a conditional electric-field criterion, which defines an apparent J_c by the relation, $U(J_c,T,B)=0$. For instance, vortex glass/collective creep models[1] give a divergent dependence $U=U_c[(J_c/J)^{\mu}-1]$ at small $J \ll J_c$, which has been observed in transport and magnetization measurements on HTS's.[3] Similar though less singular logarithmic dependence $U=U_c \ln(J_c/J)$ corresponds to power-law E-J characteristics, $E=E_c(J/J_c)^n$ with $n(T,B)=U_c/T \sim 3-30$. It is a good approximation of the observed $E(J)$ for type-II superconductors, especially for layered Bi-based HTS's.[5]

If the distribution of $\mathbf{J}(\mathbf{r})$ varies on spatial scales greater than L_c, a superconductor can be regarded as a highly nonlinear, nonuniform conductor with a local characteristic $\mathbf{E}(J,\mathbf{r})$. For example, Eqs. (1) and (2) describe nonlinear transport in superconductors with macroscopic obstacles or percolative current flow in HTS polycrystals with grain sizes $\gg L_c$ (Fig. 2). This case is important for understanding current-limiting mechanisms of HTS's, which, in addition to grain boundaries, often contain other macroscopic defects, such as second phase precipitates, microcracks, and regions of local nonstoichiometry on scales of order 10–1000 μm.[6] These current-blocking obstacles cause macroscopically nonuniform distributions of transport and magnetization currents, as revealed by magneto-optical imaging of HTS's.[7–10] In turn, even comparatively weak inhomogeneities of local $\mathbf{J}(\mathbf{r})$ can cause exponentially strong variations of the electric field, $\mathbf{E}(\mathbf{r}) \propto \mathbf{J} \exp[-U(J)/T]$, which radically change global characteristics of superconductors $\overline{J}(\overline{E},B,T)$ observed in experiment. Thus the behavior of $\overline{J}(\overline{E},B,T)$ can be different from local characteristics (1) determined by thermally activated vortex dynamics and pinning on mesoscopic scales, $L<L_c$. For instance, the relation between global $\overline{J}(\overline{E},B,T)$ characteristics and local $J(E,r)$ is rather complex, even in nonuniform Ohmic conductors.[11] This is even more so for superconductors, where the global and local characteristics can exhibit different dependencies on E, B, and T, because the nonlinearity of $E(J)$ makes the effective current-carrying cross section dependent on T, B, and E.[12–15]

Shown in Fig. 3 are examples of 2D current flows for different cases, which could be regarded as elementary ''building blocks'' of a more general percolative network in Fig. 2. The geometries shown in Fig. 3 are also quite common in experimental studies of resistive states in superconductors, thin-film superconducting electronic circuits and HTS conductors for power applications. For instance, Fig. 3(a) shows a superconducting film with a strong current-limiting planar defect (microcrack or high angle grain boundary). The case in Fig. 3(a) is also mathematically analogous to that in Fig. 3(b), which shows current flow through a faceted grain boundary with alternating segments of different J_c values. Other common geometries include the current injector (or magnetic flux transformer) [Fig. 3(c)] and the microbridge [Fig. 3(d)]. In all cases shown in Figs. 2 and 3, the electric field and current density are inhomogeneous on macroscopic scales and have singularities near the sharp edges and corners. Calculations of the global E-J characteristics then require solving Eqs. (1) and (2).

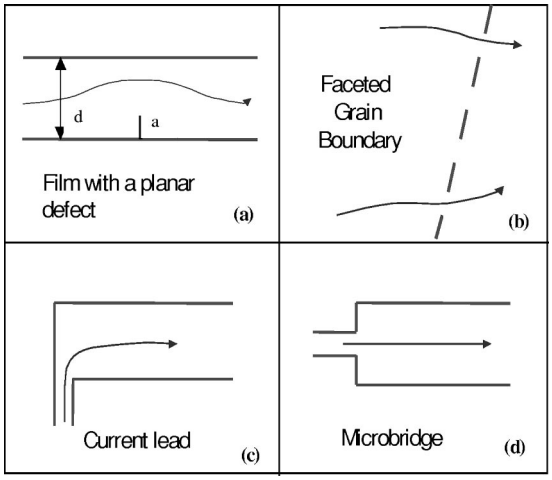

FIG. 3. Characteristic cases of the 2D nonlinear current flow solvable by the hodograph method.

The highly nonlinear Eqs. (1) and (2) represent a difficult mathematical problem, which has, to our knowledge, not so far been addressed analytically, except for a few results on 1D flux penetration[16] and flux creep dynamics.[4] Extensive numerical studies of the dynamics of flux penetration by Brandt[17] have revealed many important features of nonlinear flux dynamics in superconductors, such as narrow domain walls separating regions with different directions of current flow, nonlocal flux diffusion in thin samples, the influence of geometrical barrier, etc. On the other hand, the problem of 2D steady-state transport current flow has remained unsolved, because even numerical simulations of Eqs. (1) and (2) become exceedingly time consuming as the nonlinearity of $E(J)$ increases. For large n values, even weak spatial variations of $\mathbf{J}(\mathbf{r})$ around planar defects in Fig. 2 produce exponentially large variations of electric field $E(r)=E_c[J(r)/J_c]^n$. This fact along with singularities of $\mathbf{J}(\mathbf{r})$ and $\mathbf{E}(\mathbf{r})$ at the edges considerably complicate numerical analysis of Eqs. (1) and (2), making it necessary to develop an analytical method for solving Eqs. (1) and (2).

An approximate method for obtaining current distribution in superconductors is given by the Bean critical state model,[18,19] which replaces the real $E(J)$ curve (1) by a stepwise dependence: $\mathbf{J}=\mathbf{E}J_c/E$ for $E>0$, and $E=0$ for $J<J_c$ (Fig. 1). This model may be regarded as an extreme limit of the power-law characteristic, $E=E_c(J/J_c)^n$ for $n \to \infty$,[17] which enables analytical solutions for $\mathbf{J}(\mathbf{r})$ for some simple cases (Fig. 4). These solutions exhibit characteristic ''discon-

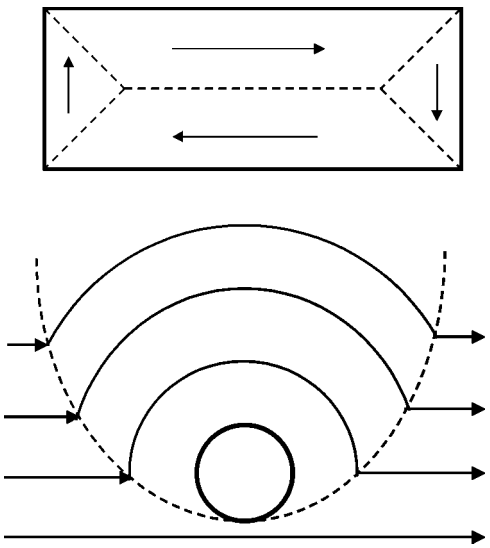

FIG. 4. Magnetization current flows predicted by the Bean model. Top: long slab in a parallel magnetic field. Bottom: current flow around a cylindrical void (Ref. 19). Dashed lines show the parabolic *d* lines, on which **J** sharply changes direction. Current streamlines between the *d* lines are circular, and centered in the void.

tinuity'' lines (*d* lines), along which the current abruptly changes direction. Another feature of this model is that finite-size defects can cause current disturbances of infinite range, as it occurs for current flow past a cylindrical void, in which case parabolic *d* lines extend to infinity[19,20] [Fig. 4(b)]. Both the zero thickness of the *d* lines and the infinite spatial scale of current perturbations are consequences of the zero resistivity for the idealized Bean's E-J characteristic in the whole interval $0<J\leqslant J_c$. In this case, solving steady-state Eqs. (2) becomes an ill-defined mathematical problem, which reduces to the only condition of current continuity, $\mathrm{div}\,\mathbf{J}=0$, provided that $J\leqslant J_c$. These conditions can be satisfied by many different current distributions for a given sample geometry, since the selection of Bean's solutions for $\mathbf{J}(\mathbf{r})$ is due to initial conditions. For example, the initial distribution of electric field $\mathbf{E}(\mathbf{r})$ can be induced by increasing external magnetic field. Once the initial conditions are fixed by the magnetic prehistory, the distribution of $\mathbf{J}(\mathbf{r})$ stays frozen indefinitely.

The inherent hysteresis of the critical state makes the Bean model inappropriate for calculations of steady-state transport current flow around planar obstacles in Figs. 2 and 3, for which the current-carrying cross section varies along a superconductor. In this case current path inevitably breaks into regions in the critical state, $J=J_c$, and subcritical regions, with $0<J<J_c$. However, the particular distribution of these regions depends on initial conditions and thus cannot be calculated by solving the steady-state equations, $\mathrm{div}\,\mathbf{J}=0$ and $J\leqslant J_c$. This unphysical situation results from the fact that the Bean model ignores the necessary condition $\nabla\times\mathbf{E}=0$, which can only be satisfied by taking account of the highly nonlinear E-J characteristics (1). Although exponentially small at $J<J_c$, the nonzero electric field plays an important role, since solving Eqs. (1) now becomes a well-defined mathematical problem, for which each nonzero value of **J** corresponds to a certain **E**. The account of E eliminates the infinite extent of current perturbations around local inhomogeneities (Fig. 4), the zero thickness of the *d* lines, and multiple solutions of the Bean model, fixing a unique steady-state transport current distribution for given boundary conditions. However, the account of the nonlinear $E(J)$ requires solving the following nonlinear equation for the scalar potential φ:

$$\mathrm{div}\left[\frac{\nabla\varphi}{|\nabla\varphi|}J(|\nabla\varphi|)\right]=0, \tag{4}$$

which is obtained by substituting $\mathbf{E}=-\nabla\varphi$ into Eq. (1) and then into $\mathrm{div}\,\mathbf{J}=0$. The 2D Eq. (4) is rather difficult to solve either analytically or numerically.

Recently we proposed an analytical method to calculate 2D steady-state transport current flow in superconductors with the account of their nonlinear $E(J)$ characteristics.[21,22] The method is based on a *hodograph* transformation, developed at the beginning of the 20th century to describe compressible gas flow.[23,24] In Ref. 21 the hodograph method was developed as to describe current flow in anisotropic superconductors. Using this method, analytical steady-state solutions of Eqs. (1) and (2) for current flow past a planar defect were obtained for the power-law E-J characteristics.[22] The essence of the hodograph method is the following. Instead of dealing with the highly nonlinear equation for $\varphi(\mathbf{r})$ in the coordinate space, we change variables and express $\varphi(\mathbf{r})$ as a function of the electric field **E**:

$$\varphi(\mathbf{r})\rightarrow\varphi(\mathbf{E}). \tag{5}$$

The hodograph transformation (5) reduces the nonlinear Eq. (4) for $\varphi(\mathbf{r})$ to a *linear* equation for $\varphi(\mathbf{E})$. In turn, the equation for $\varphi(\mathbf{E})$ can be further reduced to other well-studied linear partial differential equations, such as Thomas-Fermi or London equations, whose known solutions can be used to obtain exact solutions for 2D current flows in nonlinear conductors. For example, the nonlinear current flow around a planar defect can be mapped onto a solution of the London equation, which describes the magnetic-field distribution from a fictitious fluxon in a film with cuts. Here the nonlinearity of the power-law characteristic $E=E_c(J/J_c)^n$ manifests itself in the nonzero effective ''screening length'' $l=2\sqrt{n}/(n-1)$. These analogies enables one to use known solutions of the London, Debye, or diffusion equations (see below) to obtain analytical solutions for the 2D nonlinear current flows in superconductors with macroscopic defects.[22]

The hodograph method enables us to resolve the ambiguities of the Bean model and address analytically features of 2D nonlinear transport current flow. In particular, it gives a unique steady-state distribution $\mathbf{J}(\mathbf{r})$ for a given sample geometry and shows that current flow breaks into domains with different orientations of **J** separated by current domain walls reminiscent of the *d* lines of the Bean model. However, there are important differences between the current domain walls and the *d* lines. First of all, the domain walls have an internal structure and a varying width, which depends both on the n value and the geometry of current flow. For instance, for current flow past a void in Fig. 4, the width of the domain

walls increases with the distance from the void. It is the broadening of the domain walls, which provides the decay of current perturbations caused by the defect size a on a *finite* length $L_\perp \sim an$, much larger than a, if $n \gg 1$. Moreover, the current domain walls described by exact hodograph solutions remain different from the phenomenological d lines even in the critical state limit, $n \to \infty$. In this case current flow near domain walls exhibits no discontinuities in the tangential components of $\mathbf{J}(x,y)$ thus satisfying $\nabla \times \mathbf{E} = 0$.

In this and a subsequent paper[25] we present a detailed description of the hodograph method and calculate various steady-state 2D transport current flow in superconductors. In this paper we focus on general features of current flow in isotropic nonlinear conductors illustrated by characteristic examples, which show how the method works. We present exact solutions of Eq. (4), which reveal new length scales of nonlinear current flow and the structure of current domain walls. The second part of this work[25] is devoted to calculations of the distributions of $\mathbf{J}(\mathbf{r})$ and $\mathbf{E}(\mathbf{r})$ for restricted geometries shown in Fig. 3. Because of the long-range disturbances of the $\mathbf{E}(x,y)$ near defects in superconductors,[22] the effect of the sample geometry becomes crucial and in many cases completely dominates the global nonlinear current transport. These results enable us to calculate global E-J characteristics and dissipation due to defects, which also pertain to the problems of current-carrying capability, ac losses, and thermal stability of superconductors. In addition to superconductors, the hodograph method can also be applied to calculations of nonuniform current flow in other nonlinear media, such as semiconductors, plasma, etc. For instance, E-J characteristics of gas or semiconductor plasma at high electric fields can be approximated by the power-law dependence, $E \propto J^n$, with $n \ll 1$.[26]

The paper is organized as follows. In Sec. II we consider features of nonlinear current flow and discuss conditions, under which the steady-state current distributions in superconductors set in. In Sec. III we formulate the hodograph method and give general solutions of the hodograph equations, which then will be used to reveal features of the 2D current flows for particular geometries. In Sec. IV we consider current flow past a semi-infinite corner and calculate analytically the structure of the current domain walls and singularities in $\mathbf{J}(\mathbf{r})$ and $\mathbf{E}(\mathbf{r})$ distributions near sharp edges. In Sec. V we obtain a solution for current flow past a nonconducting planar defect in an infinite superconductor, and identify the new length scales of $\mathbf{E}(\mathbf{r})$ which are caused by the nonlinearity of $E(J)$. We describe flux flow regions near the edge of the planar defect and address a nontrivial critical state limit at $n \to \infty$. In Sec. VI we calculate excess dissipation on planar defects for nonlinear $E(J)$ characteristics. Sec. VII is devoted to the discussion of the results and their implications for nonlinear current transport and current-limiting mechanisms in HTS's.

II. NONLINEAR 2D CURRENT FLOW

A. Time scales

In this paper we consider the 2D steady-state transport current flow, which sets in after initial relaxation of current distribution induced by switching on a dc power supply. In superconductors, such transient processes can dominate the observable behavior on ''human'' time scales, because the strong nonlinearity of $J(E)$ can make the relaxation time t_0 astronomically large. In this case, the superconductor remains in a metastable critical state, which relaxes very slowly toward a true steady state. Therefore an estimation of t_0 is necessary to find the conditions, under which the steady-state current flow actually occurs.

We estimate t_0 of macroscopic current relaxation, assuming that a superconductor is in a high magnetic field, so that both self-field effects and the surface or geometrical barriers can be neglected. In this case $\mu_0 \mathbf{H} = \mathbf{B}$, and $J(E,B) = J(E,B_0)$, where B_0/μ_0 is a constant applied magnetic field. Eqs. (2) then reduce to

$$\mu_0 \sigma \partial_t \mathbf{E} = -\nabla \times \nabla \times \mathbf{E}. \tag{6}$$

Here $\sigma(E) = \partial J/\partial E$ is the differential conductivity, whose dependence on $E = |\mathbf{E}|$ determines the dynamics of $\mathbf{E}(\mathbf{r},t)$. The important feature of $\sigma(E)$ in the subcritical state ($E \ll E_c$) is an approximately inverse dependence $\sigma(E) \approx J_1/E$ for all existing models of thermally activated vortex dynamics described by Eq. (1).[4] This universality holds in a very wide region of E to the accuracy of a much weaker logarithmic variation of $J_1(E)$ at large $n \sim 3$–30. Here the parameter $J_1 = T/|\partial_J U| = sJ$ can be expressed in terms of the observed dimensionless flux creep rate, $s = d \ln J / d \ln t$.[1–4]

Since macroscopic electrodynamics of superconductors becomes model independent, when formulated in terms of the electric field $\mathbf{E}(\mathbf{r},t)$, the time scale t_0 can be estimated by a scaling analysis of Eq. (6).[4] Indeed, Eq. (6) can be regarded as a nonlinear diffusion equation for the electric field $\mathbf{E}$ with the diffusivity $D(E) = 1/\mu_0 \sigma$. Thus the time scale t_0 of current redistribution in a region of size L is given by $t_0 \sim L^2/D$, whence

$$t_0 \sim \mu_0 L^2 J_1 / E. \tag{7}$$

Here t_0 determines the duration of a transient process after which a steady-state current flow sets in. Because of the exponential dependence of E on J, the electric field E in Eq. (7) (and thus t_0) can vary strongly within a superconductor. The upper bound of t_0 can be estimated by substituting the steady-state $\mathbf{E}(\mathbf{r})$ in Eq. (7). For instance, taking the standard electric field criterion, $E_c \simeq 1 \mu V/cm$ for J_c and a characteristic spacing between defects, $L \simeq 100$ μm, we obtain $t_0 \simeq 0.06$ sec, for $J_1 = sJ_c$, $J_c = 10^6$ A/cm^2 and $s = 0.05$. In this case a steady-state transport current flow sets in on a short time scale, even for high J_c values.

However, geometrical constraints for certain sample geometries can make t_0 much larger than the above estimate. As an example, we first consider the current lead of width L_1 attached to a sample of width $L_2 > L_1$ [Fig. 3(c)], assuming the power law $E = E_c (J/J_c)^n$ with $n \simeq 3$–20. Let the lead be in a uniform critical state, ($E_1 \simeq E_c$), which sets in at $t > t_1 \simeq \mu_0 s J_c L_1^2 / E_c$. Then it takes $t > t_2 \simeq \mu_0 s J_c L_2^2 / E_2$ for a steady-state uniform current flow to occur in the sample, where E_2 is determined by the current conservation condition, $E_2 = E_1 (L_1/L_2)^n$, giving $t_2 \simeq t_1 (L_2/L_1)^{n+2}$. For $n = 15$ and $L_2 = 2L_1$, this yields $t_2 \simeq 1.3 \times 10^5 t_1$, or about 2.2 h for $t_1 = 0.06$ sec.

A similar argument can be made for the important case of a planar defect in a film [Fig. 3(a)], for which $L_2 = d$, L_1

$\simeq d-a$, where d is the film thickness, and a is the length of the defect. If the electric field near defect is of order E_c, then the electric field in the bulk, $E_2 \simeq (1-a/d)^n E_1$ can be much smaller than E_c, even for a small defect, $a \ll d$. Thus the steady-state current flow near defect sets in after $t > t_1 \simeq \mu_0 s J_c (d-a)^2/E_c$, while it can take a much longer time, $t > t_2 \sim t_1/(1-a/d)^{n+2}$ in the bulk. For $d=1$ mm, $n=15$, $J_1 = 5\times 10^4$ A/cm^2, we find that $t_1 \simeq 6.3$ sec, but $t_2 \sim 38$ sec for $a=0.1d$, $t_2 \sim 45$ min for $a=0.3d$, and $t_2 \sim 9.6$ days for $a=0.5d$. For larger a and n, relaxation toward a steady-state transport current distribution occurs on time scales well exceeding the experimental time window.

The above examples show that, although the transient relaxation of $\mathbf{J}(\mathbf{r},t)$ could be very slow for certain geometries, the steady-state transport current flow for the most cases discussed in the Introduction sets in on rather short time scales. Such relaxation is accelerated in HTS's, where flux creep is rather fast, and the n values are significantly smaller than in low-T_c superconductors.[3] In the rest of this paper we therefore consider the nonlinear steady-state 2D transport current flow in superconductors, disregarding the transient period $t < t_0$, on which steady-state $\mathbf{E}(x,y)$ is formed. The relevant time scales t_0 can be estimated from Eq. (7) for any steady-state distribution $\mathbf{E}(x,y)$.

B. Steady state

For steady-state current flow, Eqs. (2) become

$$\nabla \times \mathbf{E} = 0, \quad \nabla \times \mathbf{H} = \mathbf{J}. \tag{8}$$

To satisfy the conditions $\operatorname{div} \mathbf{J} = 0$ and $\nabla \times \mathbf{E} = 0$, for the 2D current flow in the xy plane, we introduce the scalar potential φ and the stream function ψ, related to $\mathbf{J}$ and $\mathbf{E}$ as follows:

$$J_x = \partial_y \psi, \quad J_y = -\partial_x \psi, \tag{9}$$

$$E_x = -\partial_x \varphi, \quad E_y = -\partial_y \varphi, \tag{10}$$

where $\partial_\alpha \equiv \partial/\partial\alpha$. The magnetic field $\mathbf{H}(\mathbf{r})$ is expressed in terms of $\psi(x',y')$ by the Bio-Savart law,

$$\mathbf{H}(\mathbf{r}) = \frac{1}{2\pi} \int_V \frac{\{(\mathbf{r}-\mathbf{r}') \times [\hat{\mathbf{n}} \times \nabla' \psi]\}}{|\mathbf{r}-\mathbf{r}'|^3} d^3\mathbf{r}', \tag{11}$$

where the integral is taken over the current flow regions, and $\hat{\mathbf{n}}$ is the unit vector along the z axis. The stream function ψ coincides with the normal component of the magnetic field H_n for the 2D current flow in a long cylinder or slab, but can be very different from H_n for thin films.[27–31] For Ohmic conductors, both φ and ψ satisfy the Laplace equation $\nabla^2 \varphi = 0$, $\nabla^2 \psi = 0$, so it is convenient to introduce the complex potential $w(z) = \varphi - i\rho\psi$, which is an analytic function of the complex coordinate $z = x + iy$. Here $\rho = E/J$, and the real and imaginary parts of $w(z)$ obey the boundary conditions for φ and $-\rho\psi$, respectively. This fact enables one to use powerful methods of the theory of analytic functions to calculate the 2D transport current flow in Ohmic conductors.[32] This technique is also useful for calculation of magnetization currents in superconductors.[27–29]

In nonlinear conductors the situation is much more complicated, since $w(z)$ is no longer analytic function. As a result, nonlinear current flow generally causes bulk charge density distribution, $q = \operatorname{div} \mathbf{E}$,

$$q = (\partial_J \rho)\, \mathbf{J} \nabla J, \tag{12}$$

since the resistivity $\rho = E/J$ now depends on J. For instance, for the case shown in Fig. 3(c), integration of the charge density, $q = \operatorname{div} \mathbf{E}$, gives the total charge accumulated near the current injector, $\overline{Q} = (A_1 E_1 - A_0 E_0)$. Here E_1 is the electric field in the injector, and E_0 is the electric field in the conductor, in regions far away from the joint, where both E_1 and E_0 are uniform, and A_1 and A_0 are the cross-sectional areas of the injector and the conductor, respectively. For uniform Ohmic conductors, the charge $\overline{Q}$ vanishes because $A_1 E_1 = A_0 E_0$. By contrast, for nonlinear conductors and $A_1 \neq A_0$, we get $\overline{Q} \neq 0$, since $A_1 E(I/A_1) \neq A_0 E(I/A_0)$.

The nonlinearity of $E(J)$ gives rise to new length scales for the current distribution around a local inhomogeneity. To show that, we write Eq. (4) in the form

$$\sigma_x \partial_{xx} \varphi + \sigma_y \partial_{yy} \varphi = 0, \tag{13}$$

where $\sigma_x = \partial J_x/\partial E_x$ and $\sigma_y = \partial J_y/\partial E_y$ are principal values of the differential conductivity tensor σ_{ik} calculated from Eq. (1):

$$\sigma_x = (J/E)\sin^2\theta + \sigma \cos^2\theta, \tag{14}$$

$$\sigma_y = (J/E)\cos^2\theta + \sigma \sin^2\theta. \tag{15}$$

Here $\sigma = \partial J/\partial E$ is a scalar differential conductivity, and θ is the angle between the direction of the local electric field $\mathbf{E}(x,y)$ and the x axis, so that $\tan\theta = E_y/E_x$.

For isotropic Ohmic conductors, the conductivity tensor is also isotropic, ($\sigma_x = \sigma_y$), thus the electric-field perturbations, $\delta\mathbf{E}(x,y)$, decay on a length scale of order the inhomogeneity size a, both along x and y. However, for any nonlinear isotropic $E(J)$, not only does σ_{ik} depend on $\mathbf{E}$, it also becomes highly anisotropic with respect to the current flow ($\sigma_x \neq \sigma_y$). Assuming that far away from the inhomogeneity, the current streamlines are nearly parallel to the x axis ($\theta \ll 1$), we obtain that $\sigma_x \simeq \partial J/\partial E$, and $\sigma_y \simeq J/E$. In this case, the strong nonlinearity of $E(J)$ in superconductors results in $\sigma_x \ll \sigma_y$ [for the power-law $E = E_c (J/J_c)^n$, we have $\sigma_x = \sigma_y/n \ll \sigma_y$]. The relation $\sigma_x \ll \sigma_y$ reflects the fact that the longitudinal perturbations δE_x mostly change the modulus of $J \approx J_c$, causing a rather weak current response $\delta J_x = (\partial_E J)\, \delta E_x$. By contrast, the transverse perturbations δE_y cause a local *turn* of the vector $\mathbf{J_c}$, resulting in a much larger current response $\delta J_y \simeq (J_c/E)\, \delta E_y$. The fact that $\sigma_x \ll \sigma_y$ gives rise to a decay of $\mathbf{E}(x,y)$ perturbations over very different length scales $L_\parallel$ and $L_\perp$ along the x and y axes, respectively. As follows from Eq. (13), we have $L_\perp \sim (\sigma_y/\sigma_x)^{1/2} L_\parallel$, whence

$$L_\perp \sim L_\parallel \sqrt{n}. \tag{16}$$

This relation will be illustrated below by exact solutions for particular current flows. Here we just give a simple physical estimate of $L_\perp$ and $L_\parallel$ for a planar defect of length $2a \ll d$, as shown in Fig. 3(a). The defect blocks current flow on the

length $\sim a$, forcing the current aJ_0 to redistribute around the defect on the scale $\sim L_\perp$. In the region $y<L_\perp$ the mean current density and the electric field thus increase to $J_m \sim (1+a/L_\perp)J_0$ and $E_m \sim (1+a/L_\perp)^n E_0$, respectively. The transverse decay length, $L_\perp$, is defined by the condition $E_m \sim E_0$, giving $L_\perp \sim na$. The decay length, $L_\parallel \sim a\sqrt{n}$, along current flow then follows from Eq. (16). Therefore strong ($n \gg 1$) nonlinearity of $E(J)$ greatly increases the spatial scales of electric-field perturbations, as will be confirmed below by exact calculations. At the same time, $\mathbf{E}(x,y)$ can also vary on scales much smaller than a, as it occurs in narrow current domain walls, which replace the sharp d lines of the Bean model.

III. HODOGRAPH TRANSFORMATION

A. General formalism

Instead of solving the nonlinear Eq. (13), we change variables and take φ and ψ to be functions of the complex electric field $E_x + iE_y = E\exp(i\theta)$, where θ is the polar angle between $\mathbf{E}$ and the x axis. The advantage of such a hodograph transformation is that it reduces the highly nonlinear Eq. (13) for $\varphi(x,y)$ to *linear* equations for $\psi(E,\theta)$ and $\varphi(E,\theta)$. To show this we write Eqs. (8) in the differential form,

$$d\varphi = -E_x dx - E_y dy, \quad \rho d\psi = E_y dx - E_x dy, \tag{17}$$

where $\rho(E) = E/J$. Equations (17) can be combined in a single complex equation $d\varphi - i\rho d\psi = -Ee^{-i\theta}dz$, whence

$$\partial_E z = -e^{i\theta}(\partial_E \varphi - i\rho\partial_E \psi)/E, \tag{18}$$

$$\partial_\theta z = -e^{i\theta}(\partial_\theta \varphi - i\rho\partial_\theta \psi)/E. \tag{19}$$

Here $z = x + iy$ is the complex coordinate, and $\sigma(E) = \partial J/\partial E$ is the differential conductivity (notice that in nonlinear conductors $\rho \neq 1/\sigma$). The condition $\partial^2_{\theta E} z = \partial^2_{E\theta} z$ then gives the following relations between partial derivatives of ψ and φ:

$$\partial_\theta \varphi = -(E^2/J)\partial_E \psi, \quad \partial_E \varphi = (E\sigma/J^2)\partial_\theta \psi. \tag{20}$$

Equating the mixed derivatives, $\partial^2_{\theta E} = \partial^2_{E\theta}$, for ψ and φ, we obtain the following *linear* equations for ψ and φ valid for any nonlinear dependence $J(E)$:

$$\frac{\sigma E}{J^2}\frac{\partial^2 \psi}{\partial \theta^2} + \frac{\partial}{\partial E}\left(\frac{E^2}{J}\frac{\partial \psi}{\partial E}\right) = 0, \tag{21}$$

$$\frac{J}{E^2}\frac{\partial^2 \varphi}{\partial \theta^2} + \frac{\partial}{\partial E}\left(\frac{J^2}{\sigma E}\frac{\partial \varphi}{\partial E}\right) = 0. \tag{22}$$

For the power-law dependence, $E = E_c(J/J_c)^n$, these equations simplify to

$$\frac{J^2}{n}\frac{\partial^2 \psi}{\partial J^2} + J\frac{\partial \psi}{\partial J} + \frac{\partial^2 \psi}{\partial \theta^2} = 0, \tag{23}$$

$$nE^2\frac{\partial^2 \varphi}{\partial E^2} + E\frac{\partial \varphi}{\partial E} + \frac{\partial^2 \varphi}{\partial \theta^2} = 0. \tag{24}$$

In Eq. (23) we can change variables, $E = E_c(J/J_c)^n$, and express ψ as a function of E and θ, which is convenient for the further analysis of electric-field distributions. Equations (23) and (24) can also be presented in different useful forms by introducing new variables,

$$\varphi = e^{\beta\eta}h_1, \quad \psi = e^{-\beta\eta}h_2, \quad \eta = \frac{1}{\sqrt{n}}\ln\frac{E}{E_0}. \tag{25}$$

Here E_0 is the electric field at infinity, and the functions $h_{1,2}(\eta,\theta)$ satisfy the equation,

$$\partial^2_{\eta\eta}h + \partial^2_{\theta\theta}h - \beta^2 h = 0, \tag{26}$$

which has the form of the London equation with the inverse ''screening length'' β:

$$\beta = (n-1)/2\sqrt{n}. \tag{27}$$

Therefore the nonlinearity of $E(J)$ results in an effective screening of $\psi(\eta,\theta)$ in the hodograph space, which becomes stronger as n increases. For $n=1$, Eq. (26) turns into the Laplace equation, thus the complex potential $w(u) = \varphi - i\rho\psi$ is an analytic function of $u = \eta - i\theta$ in the hodograph representation. Analytic properties of the complex potential $w(\eta,\theta)$ in nonlinear conductors are considered in Appendix A. We show that for $n>1$, $w(\eta,\theta)$ is no longer analytic function, but can be expressed in terms of generalized analytic functions.[33]

B. Solving the hodograph equations

The calculation of nonlinear current flow by the hodograph method is implemented in two steps. First, a solution of the linear Eq. (21) should be found, which satisfies the particular boundary conditions. Then an inverse transformation of $\psi(\theta,E)$ from the hodograph plane (E,θ) onto the physical xy plane should be performed to obtain the current streamlines $\psi = \psi(x,y)$ and spatial distributions of the electric fields and currents. As shown in Appendix E, the Jacobian of the inverse transformation does not change sign for any isotropic E-J characteristic with positive differential conductivity $\sigma(E)$.[21] This fact makes the hodograph transformation a well-defined procedure, for which each solution $\psi(E,\theta)$ corresponds to a unique spatial distribution of $\mathbf{E}(x,y)$ for given boundary conditions.

Solutions of Eqs. (21) and (22) can be obtained by separating variables as follows:

$$\psi(E,\theta) = \sum_m C_m f_m(E)\sin(m\theta + \phi_m). \tag{28}$$

Here C_m and ϕ_m are constants, and the functions $f_m(E)$ satisfy the following ordinary differential equation:

$$\frac{d}{dE}\left(\frac{E^2}{J}\frac{df_m}{dE}\right) - \frac{m^2\sigma E}{J^2}f_m = 0. \tag{29}$$

An analogous expression to Eq. (28) for the electric potential $\varphi(E,\theta)$ can be obtained with the eigenfunctions $g_m(E)$ satisfying

$$\frac{d}{dE}\left(\frac{J^2}{\sigma E}\frac{dg_m}{dE}\right)-\frac{m^2 J}{E^2}g_m=0. \tag{30}$$

For the power-law $J(E)$ characteristic, Eq. (23) gives $f_m(E)\propto E^{q_m}$, so $\psi(E,\theta)$ takes the form

$$\psi(E,\theta)=\psi_0+[B_1+B_2(E/E_0)^{1/n-1}](\theta+\theta_0)+\sum_m C_m^{\pm}\left(\frac{E}{E_0}\right)^{q_m^{\pm}}\sin(m\theta+\phi_m), \tag{31}$$

$$q_m^{\pm}=\frac{1}{2n}[1-n\pm\sqrt{(n-1)^2+4nm^2}]. \tag{32}$$

Here the sum runs over all integer m, the constants $B_{1,2}$, $C_m^{\pm}$, ψ_0, θ_0, E_0, and ϕ_m are determined by the boundary conditions, and E_0 can be taken as the electric field at infinity. We emphasize that Eqs. (31) and (32) are *exact* general solutions of the nonlinear Maxwell equations which describe various current flows.

If distributions $\mathbf{E}(x,y)$ contain regions of $E<E_0$ and $E>E_0$, with different sets of $C_m^{(+)}$, $q_m^{(+)}$, and $C_m^{(-)}$, $q_m^{(-)}$, the solutions $\psi_+(E,\theta)$ for $E>E_0$ and $\psi_-(E,\theta)$ for $E<E_0$ should be matched at $E=E_0$ as to provide continuity of $\psi(E,\theta)$ and its derivatives. Finding the proper relation between $C_m^{(+)}$ and $C_m^{(-)}$ can be reduced to the solution of the following linear matrix equation:[25]

$$\sum_k U_{mk}C_k=F_m, \tag{33}$$

where U_{mk} and F_m are determined by the sample geometry. The fact that both $\psi_-(E,\theta)$ and $\psi_+(E,\theta)$ are known exactly is a great advantage of the hodograph method, which thus reduces the initial nonlinear problem to a standard procedure of matrix inversion. In some cases the coefficients C_m can be obtained analytically, otherwise $C_m=\Sigma_k U_{km}^{-1}F_k$ can be effectively calculated numerically.[25] Since the hodograph method linearizes the Maxwell equations for any $E(J)$, numerical calculations of nonlinear current flow $\mathbf{J}(x,y)$ for the cases shown in Figs. 2 and 3 take no longer than the corresponding calculations of $\mathbf{J}(x,y)$ for Ohmic conductors.

The solution (31) is rather convenient for performing the inverse transformation of $\psi(E,\theta)$ onto the coordinate space xy, giving the electric-field distribution $z=z(E,\theta)$ for any set of $C_m^{\pm}$. This is a well-defined mathematical procedure, since the Jacobian of the inverse transformation is always positive for any isotropic E-J characteristic, as shown in Appendix E. To obtain $\mathbf{E}(x,y)$, we exclude $\partial_E\varphi$ and $\partial_\theta\varphi$ from Eqs. (20), which yields

$$\partial_\theta z=\frac{e^{i\theta}}{J}(E\partial_E\psi+i\partial_\theta\psi), \tag{34}$$

$$\partial_E z=\frac{e^{i\theta}}{J}\left(i\partial_E\psi-\frac{\sigma}{J}\partial_\theta\psi\right). \tag{35}$$

Substituting Eq. (31) into Eq. (35) and integrating over E, we obtain

$$z=z_{\pm}+e^{i\theta}\left(\frac{B_1}{J}+\frac{B_2E_0}{nE}[1+i(n-1)(\theta+\theta_0)]\right)-\frac{e^{i\theta}}{J}\sum_{m=0}^{\infty}\frac{C_m^{\pm}}{nq_m^{\pm}-1}\left(\frac{E}{E_0}\right)^{q_m^{\pm}}(m\cos\vartheta_m-inq_m^{\pm}\sin\vartheta_m). \tag{36}$$

Here $z_{\pm}$ are constants, $\vartheta_m=m\theta+\phi_m^{\pm}$, and the plus and the minus signs correspond to $E<E_0$ and $E>E_0$, respectively. Equations (36) represent a complete family of exact solutions of nonlinear Maxwell's equations for various distributions $\mathbf{E}(x,y)$, parameterized by an infinite set of constants C_m. In the following sections we will show how C_m can be found for particular current flows.

Equation (26) belongs to the well-studied linear equation of mathematical physics, so various nonlinear current distributions can be obtained from known solutions for other physical problems described by the London or diffusion equations. For instance, a solution $\psi(\eta,\theta)$ of Eq. (23) inside the region bound by the contour S in the hodograph plane $\eta\theta$ can be expressed in terms of the surface distribution $\psi_b(s)$:

$$\psi(\eta,\theta)=e^{-\beta\eta}\oint_S e^{\beta\eta'}\psi_b(s)\partial_n G(\eta,\eta',\theta,\theta')ds. \tag{37}$$

Here $\psi(\eta,\theta)$ is determined by the boundary conditions, the Green's function G of Eq. (26) satisfies the boundary condition $G=0$ on S, and ∂_n denotes the normal derivative on S. The function G has a clear physical meaning, since it is proportional to the local magnetic field at the point η,θ produced by a fictitious London vortex located at the point η',θ' in a superconducting cylinder. This analogy enables one to use extensive results on vortices in superconductors of different geometries to calculate $G(\eta,\eta',\theta,\theta')$ and thus 2D current flows in nonlinear conductors.[22]

Another analogy follows from the following representation of Eqs. (23) and (24):

$$\partial_{\theta\theta}^2\psi+\partial_{\eta\eta}^2\psi+2\beta\partial_\eta\psi=0, \tag{38}$$

$$\partial_{\theta\theta}^2\varphi+\partial_{\eta\eta}^2\varphi-2\beta\partial_\eta\varphi=0. \tag{39}$$

Equations (38) and (39) have the form of diffusion equations, which describe steady-state distributions of the fields ψ or φ in a reference frame moving with the velocity $\pm 2\beta$. Equations (38) and (39) also belong to the well-studied linear equations,[34] which could help on finding solutions of the hodograph equations, using the known solutions of the corresponding diffusion problems. For instance, in the critical state limit ($n\to\infty$), Eq. (23) becomes a simple 1D diffusion equation in the hodograph space

$$\partial_\tau\psi=\partial_{\theta\theta}\psi, \tag{40}$$

where $\tau=\ln(J_c/J)$ and θ play the roles of ''time'' and ''coordinate,'' respectively. In this case the solution of Eq. (40) for the stream function

$$\psi=B\theta+\sum_{m=1}^{\infty}C_m\left(\frac{J}{J_c}\right)^{m^2}\sin(m\theta+\phi_m) \tag{41}$$

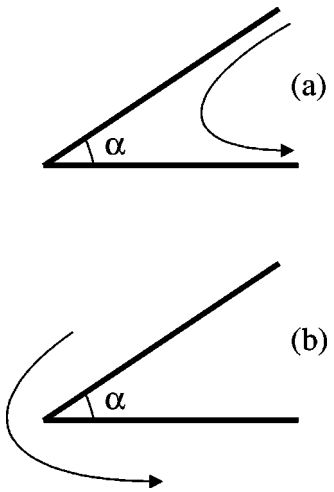

FIG. 5. Inner (a) and outer (b) current flows around a corner.

is independent of n and therefore can be regarded as a ''critical state'' limit for $\psi(J,\theta)$. However, as will be shown below, Eq. (41) can result in current distributions, which are different from those of the Bean model.

C. Boundary conditions

To take advantage of the exact solutions for $\psi(E,\theta)$ and $\varphi(E,\theta)$, we need to reformulate the corresponding boundary conditions in the hodograph space. This procedure is rather nontrivial, since even simple boundary conditions in the xy plane, such as zero normal component of **J** on the sample surface, or a given distribution of **J** or **E** on the electrodes, can become highly nonlinear in the $E\theta$ plane. For instance, if current flows past a cylindrical void of radius R, the condition of zero normal component of $\mathbf{J}(x,y)$ requires constant $\psi(x,y)=\psi_0$ on the surface, $x^2+y^2=R^2$. Taking the hodograph solutions $x=A(E,\theta), y=B(E,\theta)$, we obtain the boundary conditions in the $E\theta$ plane: $A^2(E,\theta)+B^2(E,\theta)=R^2$ and $\psi(E,\theta)=\psi_0$. Substituting here Eq. (36), we arrive at an infinite set of coupled nonlinear equations for C_m and ϕ_m. Therefore the boundary conditions become nonlinear for curved boundaries or nonuniform distributions of $\mathbf{J}(x,y)$ on the electrodes.

However, for any 2D current flow confined between flat, piece-wise boundaries, or around planar cuts (see Figs. 2 and 3), the boundary conditions in the hodograph space greatly simplify. Then the condition of zero normal component of **J** at the straight boundary inclined by the angle θ_0 becomes linear, reducing to $\psi(E,\theta_0)=\psi_0$, where ψ_0 is a constant. For example, for current flow around a corner shown in Fig. 5, the boundary conditions can be taken in the form, $\psi(E,0)=\psi(E,\alpha)=0$. Therefore, for current flow around planar obstacles, the hodograph transformation linearizes both the equation for $\psi(E,\theta)$ and the boundary conditions. In this case we can obtain complete exact solutions of the nonlinear Maxwell equations considered in the following sections.

IV. CORNER

One of the simplest exact solutions of Eq. (23) describes current flow around a corner. There are two different situations which we consider separately, corresponding to current flow inside or outside of two unpenetrable walls inclined at the angle α (Fig. 5). This case allows us to calculate structure of the current domain walls and trace the nonanalytic crossover from large, but finite n value, to the critical state limit $n\to\infty$.

A. General solution

The solution for current flow around the corner, satisfies the boundary conditions, $\psi(E,0)=\psi(E,\alpha)=0$, corresponding to zero normal component of **J** on the sample surface. This solution of Eq. (23) has the form

$$\psi = CE^q \sin k\theta, \tag{42}$$

where $k=\pi/(\pi-\alpha)$, C is a scaling constant, and

$$q_k^{\pm}=\frac{1}{2n}[1-n\pm\sqrt{(1-n)^2+4nk^2}]. \tag{43}$$

Here the plus and the minus signs correspond to current flow inside and outside the region of the angle α, respectively (Fig. 5). Taking the origin, $z=0$, as the vertex for both cases, we obtain the distribution of $\mathbf{E}(x,y)$, substituting Eq. (42) into Eq. (35) and integrating from 0 to E for $q=q^+$ and from ∞ to E for $q=q^-$. This yields

$$z=-\frac{Ce^{i\theta}E^q}{(qn-1)J(E)}(k\cos k\theta - iqn\sin k\theta). \tag{44}$$

Separating real and imaginary parts of Eq. (44), and excluding E by dividing $y(E,\theta)$ by $x(E,\theta)$, we obtain the following equation for the function $\theta(x,y)$, which determines local orientation of current flow

$$\frac{y}{x}=\frac{k\tan\theta - nq_k\tan k\theta}{k+nq_k\tan\theta\tan k\theta}. \tag{45}$$

We use these results to consider two particular cases: (i) Current flow past a semi-infinite cut, for which $q=-1$, $\alpha\to 0$; (ii) Current flow near a rectangular corner, for which $q=q_2^{\pm}$, $\alpha=\pi/2$. In the first case, $\psi=C\sin\theta/E$ is independent of n, and Eq. (44) gives

$$z=\frac{Ce^{i\theta}}{(n+1)JE}(\cos\theta+in\sin\theta). \tag{46}$$

Current streamlines described by Eqs. (42) and (46) are shown in Fig. 6. For $n\gg 1$, current streamlines are approximately semicircles centered near the end of the cut, while contours of constant electric field are close to circles which cross the cut. Near the edge, $(x\approx 0, y=0)$, the electric field $E(x)$ has a singularity. For $x<0$ and $y\to\pm 0$, currents flow parallel to the cut [$\theta=0$ at $y=+0$, or $\theta=\pi$ at $y=-0$, (see Fig. 6)], and Eq. (46) gives $x=C/(n+1)JE$. For $x>0$, we have $\theta=\pi/2$, and $x=-nC/(n+1)JE$, whence

$$E(x)\propto 1/nx^{n/(n+1)}, \quad x<0, \tag{47}$$

$$E(x)\propto 1/x^{n/(n+1)}, \quad x>0. \tag{48}$$

Hence the circle of constant E of radius R crosses the cut at the point $\simeq R/n$ away from the edge. For the linear case, $n=1$, Eq. (48) gives the square-root singularity $J(x)$

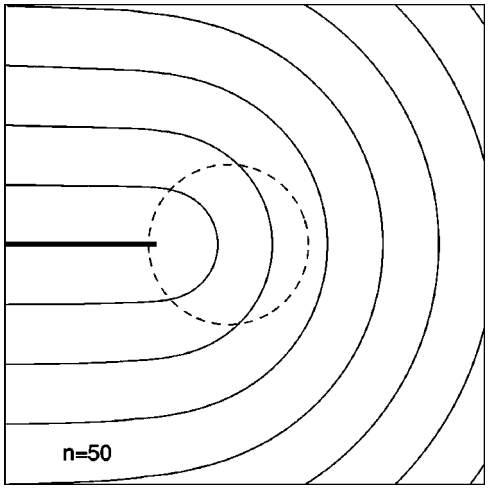

FIG. 6. Nonlinear current flow around a semi-infinite cut. Dashed circle shows a contour of constant electric field. For $n \to \infty$, all circular contours of constant E touch the end of the cut.

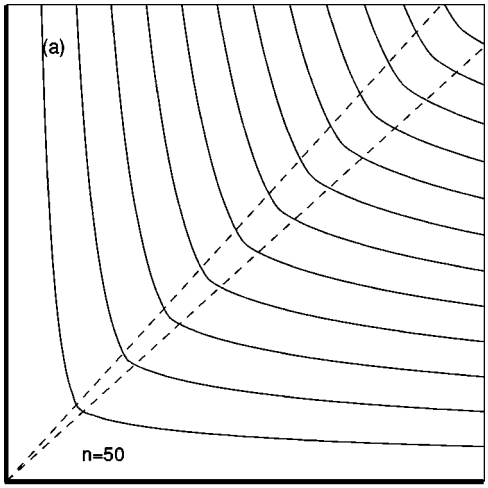

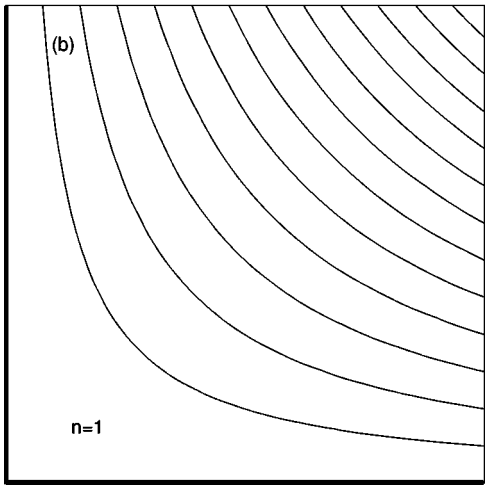

FIG. 7. Current flow near the corner of a rectangular sample for a superconductor ($n=50$) (a) and a normal metal (b). The dashed straight lines in (a) show boundaries of a diverging current domain wall, defined as a region where $|\theta-\pi/4|<0.3$.

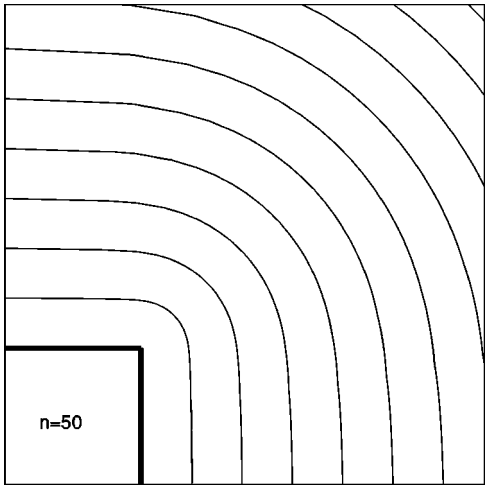

FIG. 8. Nonlinear current flow around a corner. For $n \gg 1$, current streamlines in the upper right quadrant are nearly circular, and centered in the vertex.

$=\sigma E(x) \propto 1/|x|^{1/2}$, both in $J(x)$ and $E(x)$ at $|x| \to 0$.[24,32] For $n \gg 1$, the nonlinearity of $J(E)$ in superconductors enhances the singularity in $E(x) \propto 1/|x|$, while strongly suppressing the singularity in $J(x) \propto 1/|x|^{1/n}$. For the semiconductor-type nonlinearity, $n \ll 1$, the situation is the opposite: the singularity in $E(x)$ is suppressed, but enhanced in $J(x)$.

The second example is the rectangular corner shown in Figs. 7 and 8. There are two different cases of current flow inside and outside the corner, which correspond to $q=q_2^+ > 0$ and $q=q_2^- < 0$ in Eq. (42), respectively. Excluding E from Eqs. (42) and Eq. (44), we obtain the current streamlines $x=\mathrm{Re}\, z(\psi,\theta)$ and $y=\mathrm{Im}\, z(\psi,\theta)$ in the form[22]

$$z = D\left(\frac{\psi}{\sin 2\theta}\right)^{1-1/nq_2^+} (2\cos 2\theta - inq_2^+ \sin 2\theta) e^{i\theta}, \quad (49)$$

where $D=C^{1/nq_2^+} E_0^{1/n}/J_0(nq_2^+-1)$. Each streamline corresponds to a contour of constant ψ. The evolution of the current distribution with n is shown in Fig. 7. For $n=1$, we have $q_2^+=2$, thus Eq. (49) gives smooth hyperbolic streamlines, $\psi \propto xy$.[24,32] By contrast, the highly nonlinear case $n \gg 1$ exhibits sharp changes of the current flow direction near the diagonal somewhat reminiscent of, yet different from the piece-wise current distribution of the Bean model (see below).

Current flow past the corner in Fig. 8 exhibits quite different characteristics which manifest themselves in the distribution of local orientations, $\theta(x,y)$. For $n \gg 1$ Eq. (43) gives $nq_k^- \approx -(n+k^2-1)$, thus Eq. (45) simplifies to $x/y = -\tan\theta$. The relation $x/y=-\tan\theta$ describes circular current streamlines centered in the vertex and is valid everywhere, except for narrow regions of angles, $\delta\theta \simeq n^{-1/2}$, near $\theta=0$ and $\theta=\pi-\alpha$, which correspond to currents flowing almost parallel to the sample surface. Therefore current flow around the semi-infinite corner described by exact Eq. (45) exhibits no trace of singular d lines characteristic of the case shown in Fig. 7(a).

The solutions of this subsection contain a scaling constant C, which remains undetermined for semi-infinite samples. If the corner is a part of a defect in a finite sample, say, a

surface notch or a step in a film, the above solutions describe current flow only near the corner. The constant C is determined by current distribution far away from the defect and thus depends on the sample geometry and the boundary conditions (see below). Here we just note that the particular value of C does not affect the shape of the current stream lines described by the function $\theta(x,y)$. This fact enables us to investigate universal features of the current domain walls, based on the exact, yet simple solutions (42)–(45), regardless of the particular geometry of the whole sample.

B. Structure of the current domain wall

The principal question is how the singular d line emerges in a smooth current distribution as $n\to\infty$. For the Bean model, the d line manifests itself in a step-wise change of the current orientation, $\theta(x,y)=\pi[\mathrm{sgn}(x-y)-1]/4$, as seen in Fig. 4(a). Although such a step-wise current configuration satisfies the critical state assumption, $J=J_c$, and the continuity of the normal component of $\mathbf{J}$, it has a jump of tangential component $J_\parallel$ along the d line. Thus this model distribution of $\mathbf{J}(x,y)$ cannot exist in steady state, if any electric field caused by current flow is taken into account. Indeed, a jump in $J_\parallel$ on the d line would result in a discontinuity of the tangential component of $\mathbf{E}$, which violates $\nabla\times\mathbf{E}=0$.

For finite $n\gg1$ this discontinuity is smoothed out, and the d line turns into a current domain wall of finite thickness between regions with different orientations of current flow, as follows from extensive numerical simulations performed by Brandt.[17] Here we address the following questions, which are rather difficult to resolve through numerical simulations: (i) Is there any intrinsic width of the current domain wall, which is determined by the nonlinearity of $J(E)$ regardless of the sample geometry? (ii) Is there an analytic crossover from large, but finite n to the Bean model behavior at $n\to\infty$? (iii) Is the d line of the Bean model a true steady state in the limit $n\to\infty$? (iv) Is there any singularity in current domain wall in the limit $n\to\infty$?

The exact hodograph solutions show that only the last proposition is true, while the very existence of the d line depends on the geometry of current flow. For example, the Bean model predicts the d lines for current flow both inside and outside a corner, depending on the magnetic prehistory. The results of the previous subsection indicate that, although some sort of singularity on the diagonal remains for the inside flow in Fig. 7(a), the outside flow in Fig. 8 always exhibits nonsingular circular streamlines. The latter solution also satisfies the Bean model. Therefore we see that even exponentially weak electric field in the critical state ($n\gg1$) drives the step-wise current distribution in Fig. 4(a) into the nonsingular one in Fig. 7(a), corresponding to the true steady state.

We now consider the structure of the current domain wall in Fig. 7(a) in more detail by analyzing the behavior of the function $\theta(x,y)$ near the diagonal, where $x\approx y$, $\theta=-\pi/4+\delta$, and $\delta\ll1$. If $n\gg1$, we have $nq_k^+\approx k^2-k^2(k^2-1)/n$, so Eq. (45) for $\delta\ll1$, simplifies to

$$\frac{x-y}{x}=2\delta\left(\frac{3}{n}+\delta^2\right). \tag{50}$$

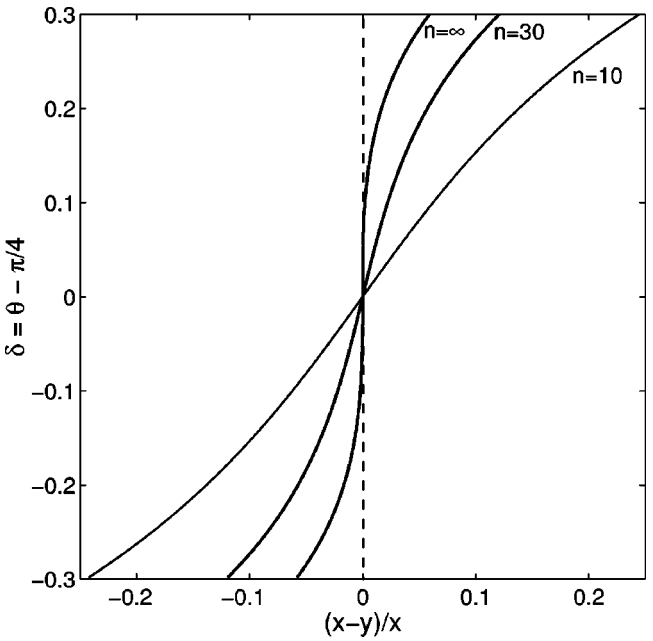

FIG. 9. Structure of the current domain wall for different n values. The dashed line shows the step-wise dependence $\delta(x,y)$ of the Bean model.

From Eq. (50) it follows that there is no ''intrinsic'' width of the current domain wall, since $\delta(x,y)$ is a power-law function of x and y near the diagonal. If we define the domain wall as a region, in which $\delta<\delta_0$, then Eq. (50) gives its width, $d(l_\parallel,\delta_0)$, as a function of the conditional criterion δ_0 and the distance $l_\parallel=(x+y)/2$ from the vertex along the diagonal. We thus obtain that the so-defined width of the current domain wall, $d=\delta_0(3/n+\delta_0^2)l_\parallel$ linearly increases with $l_\parallel$ and remains finite even in the limit $n\to\infty$. The dependence of $\theta(l_\parallel,l_\perp)$ on the coordinate $l_\perp=(x-y)/2$ across the d line at a fixed distance $l_\parallel$ from the vertex is shown in Fig. 9. For finite n, we obtain that $\delta=nl_\perp/3l_\parallel$ is linear when $l_\perp\ll l_\parallel(3/n)^{3/2}$ and acquires the universal dependence $\delta=(l_\perp/l_\parallel)^{1/3}$ when $l_\perp\gg l_\parallel(3/n)^{3/2}$. Therefore the exact theory predicts continuous broadening of the d line with $l_\parallel$, as observed in magneto-optical experiments.[7]

In the limit $n\to\infty$, we have $\delta=(l_\perp/l_\parallel)^{1/3}$ for all $l_\perp$, thus the function $\theta(l_\perp)$ remains continuous at $l_\perp=0$, but the derivative $\partial\theta/\partial l_\perp\propto l_\perp^{-2/3}$ diverges, in stark contrast to the jump in $\theta(x,y)$ for the Bean model. Such a ''soft'' singularity in $\theta(x,y)$ is rather difficult to reveal in numerical simulations of nonlinear Maxwell's equations in the coordinate space. Therefore, for $n\to\infty$, some kind of singular d lines do appear, but the behavior of $\theta(l_\parallel,l_\perp)$ turns out to be quite different from the Bean model (see Fig. 9). This difference is due to the fact that the hodograph solutions satisfy the condition $\nabla\times\mathbf{E}=0$, even for $n\to\infty$.

V. PLANAR DEFECT IN AN INFINITE SUPERCONDUCTOR

Now we consider a more complicated problem of current flow past a thin nonconducting planar defect of length $2a$ in an infinite media (Fig. 10). This case models the strongest current-limiting defects in HTS's, such as high-angle grain

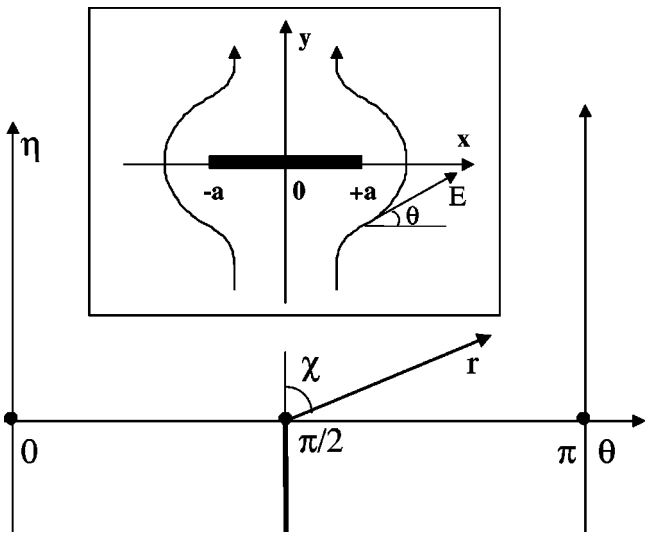

FIG. 10. Mapping of the current flow around a thin nonconducting strip in the xy plane (inset) onto the hodograph plane $\eta\theta$.

boundaries, or microcracks. To capture the general features of $\psi(\eta,\theta)$, we first consider the complex potential $w(z)$ for the same geometry in the case of Ohmic conductors,[24]

$$w = iE_0\sqrt{z^2-a^2}. \tag{51}$$

Expressing w via the complex electric field, $E\exp(-\imath\theta) = -dw/dz$ (see Appendix A), we obtain

$$w = -\frac{aE_0}{\sqrt{1+\exp 2(\eta - i\theta)}}, \tag{52}$$

where $\eta = \ln(E/E_0)$. As follows from Eq. (52), the stream function $\psi = \mathrm{Im}(w)$ has a singularity at $\eta = 0$, $\theta = \pi/2$ and decays exponentially away from this point, on the scale $\eta \sim 1$, $\theta - \pi/2 \sim 1$.

The boundary conditions for $\psi(\eta,\theta)$ in the hodograph plane follow from the symmetry properties of the current flow around the defect (Fig. 10). First, we notice that the zero x component of **J** on the central line (perpendicular to the defect) requires the boundary condition $\psi(\eta,\pi/2) = 0$. Along the ray $x = 0, -\infty < y < 0$, the electric field varies from its value at infinity, $E = E_0$, to zero at the stagnation point, $z = 0$, in the center of the planar defect. Furthermore, the zero normal component of **J** on the defect surface also requires $\psi(\eta,0) = \psi(\eta,\pi) = 0$, with E changing from 0 at $z = 0$ to infinity at the edges ($z = \pm a$). In the hodograph plane (η,θ), these boundary conditions give $\psi = 0$ along two vertical lines at $\theta = 0$ and $\theta = \pi$ and along the half-infinite line $-\infty < \eta < 0$ at $\theta = \pi/2$ (Fig. 10). Along the ray, $\eta > 0$, $\theta = \pi/2$, we have $\partial_\theta \psi = 0$. Therefore the problem reduces to the solution of the London Eq. (26) that describes a ''vortex'' at the end of the half-infinite cut, in the center of a superconducting film of thickness π. The nonlinearity results in effective ''screening'' in Eq. (26), making $h(\eta,\theta)$ more localized near the end of the cut in Fig. 10. For $n \gg 1$, $h(\eta,\theta)$ decays exponentially over the scale $\sim 1/\beta \ll 1$, so the influence of the boundary conditions on $h(\eta,\theta)$ at $\theta = 0$, π becomes very weak. In this case it is convenient to write Eq. (26) in polar coordinates (r,χ), with the origin at the end of the cut, $\eta = 0$, $\theta = \pi/2$:

$$\partial_{rr}h + r^{-1}\partial_r h + r^{-2}\partial_{\chi\chi}h - \beta^2 h = 0, \tag{53}$$

where $\eta = r\cos\chi$, $\theta = \pi/2 + r\sin\chi$, and β is given by Eq. (27).

If $\pi\beta \to \infty$, the function $h(r,\chi)$ describes a vortex at the end of the cut in an infinite media. In this case, an exact vortex solution of Eq. (53) is

$$h = \sqrt{2}h_0\frac{e^{-\beta r}}{\sqrt{r}}\cos\frac{\chi}{2}. \tag{54}$$

Solutions with higher order harmonics $\propto \cos m\chi/2$, give unphysical distributions $\mathbf{J}(x,y)$, which we do not consider here.

To satisfy the boundary condition $\psi = 0$ at $\theta = 0,\pi$, for finite β, we use the method of images, by presenting ψ as a superposition of the fields of alternating vortices and antivortices at $\eta = 0$, $\theta = \theta_m = \pi(m + 1/2)$, where $m = 0, \pm 1, \ldots$. This yields

$$\psi = h_0\sum_m (-1)^m\frac{\sqrt{r_m+\eta}}{r_m}e^{-\beta(r_m+\eta)}, \tag{55}$$

where $r_m = \sqrt{\eta^2 + (\theta-\theta_m)^2}$, and h_0 is a scaling constant, which will be obtained below. For $n \gg 1$, the sum in Eq. (55) converges very rapidly, since $\exp(-\beta\pi) \ll 1$, thus we can retain only nearest neighbors ($m = 0, \pm 1$).

Now we come back to the general Eq. (31), in which $B_{1,2} = \phi_m = 0$ by symmetry, and C_m are just the Fourier coefficients of the function $\psi(E_0,\theta)$:

$$C_m = \frac{4}{\pi}\int_0^{\pi/2}\psi(E_0,\theta)\sin m\theta\, d\theta. \tag{56}$$

For $n \gg 1$, $\psi(E_0,\theta)$ is localized around $\theta = \pi/2$, so we extend the upper limit in Eq. (56) to infinity and retain only the term with $m = 0$ in Eq. (55). Then $\psi(E_0,\theta) = h_0\exp(-\beta|\theta - \pi/2|)/\sqrt{|\theta-\pi/2|}$, and Eq. (56) gives $C_m = (4h_0/\sqrt{\pi})\mathrm{Im}[\exp(im\pi/2)/\sqrt{\beta - im}]$, whence

$$C_{2k} = h_0\frac{2^{3/2}(-1)^k}{\sqrt{\pi}\alpha_{2k}}\sqrt{\alpha_{2k}-\beta}, \tag{57}$$

$$C_{2k-1} = h_0\frac{2^{3/2}(-1)^k}{\sqrt{\pi}\alpha_{2k-1}}\sqrt{\alpha_{2k-1}+\beta}, \tag{58}$$

where $\alpha_m = \sqrt{\beta^2 + m^2}$, and k is any integer. To satisfy the boundary condition $\psi(\eta,\pi/2) = 0$ for $E < E_0$, we take $m = 2k$ in Eq. (31). For $E > E_0$, we have $\partial\psi/\partial\theta = 0$ at $\theta = \pi/2$, hence $m = 2k-1$. As a result, Eq. (31) can be presented in the form

$$\psi = \sum_{k=1}^{\infty} C_{2k}\left(\frac{E}{E_0}\right)^{q_{2k}^+}\sin 2k\theta, \quad E < E_0, \tag{59}$$

$$\psi=\sum_{k=1}^{\infty} C_{2k-1}\left(\frac{E_0}{E}\right)^{|q_{2k-1}^-|}\sin(2k-1)\theta, \quad E>E_0. \tag{60}$$

To transform $\psi(E,\theta)$ back onto the xy plane, we substitute Eqs. (59) and (60) into Eq. (35). Since $E=0$ at $z=0$, we obtain $z(E,\theta)$ in the region of $E<E_0$, integrating Eqs. (35) over E from 0 to E:

$$z=-\frac{e^{i\theta}}{J_0}\sum_{k=1}^{\infty}\frac{C_{2k}}{nq_{2k}^+-1}\left(\frac{E}{E_0}\right)^{q_{2k}^+-1/n} \times[2k\cos 2k\theta - inq_{2k}^+\sin 2k\theta], \quad E<E_0. \tag{61}$$

In the region where $E>E_0$, we use the fact that $E=\infty$ at $z=a$. Substituting Eq. (60) into Eq. (35) and integrating over E from ∞ to E, we obtain for $E>E_0$:

$$z=a+\frac{e^{i\theta}}{J_0}\sum_{k=1}^{\infty}\frac{C_{2k-1}}{n|q_{2k-1}|+1}\left(\frac{E_0}{E}\right)^{|q_{2k-1}^-|+1/n} \times[(2k-1)\cos(2k-1)\theta+in|q_{2k-1}|\sin(2k-1)\theta]. \tag{62}$$

The constant h_0 calculated in Appendix B is determined by the self-consistency condition $z(+0,0)=z(-0,0)$, which gives for $n\gg 1$

$$h_0=J_0an^{3/4}/\sqrt{2\pi}. \tag{63}$$

The current flow described by Eqs. (59)–(63) is very different from that of Ohmic conductors (Fig. 11).[35] The most visible manifestation of nonlinearity is the long-range disturbance of current streamlines on the scales much larger than the defect size, $2a$. If $n\to\infty$, the magnitude of $J(x,y)=J_c$ remains approximately constant everywhere, but a region near the central line, $x=0$. In addition, the vector **J** changes the direction at diverging current domain walls, reminiscent of the d lines for magnetization current flow past a cylindrical hole in the Bean model (Fig. 4). For finite n, the width of the current domain walls increases as the distance from the strip increases, providing the decay of current perturbations on the scale $L_\perp\gg a$.

Spatial scales of nonlinear current flow around the strip can be obtained by considering electric-field distributions along two symmetry lines: in the plane of the defect ($y=0$, $x>a$, $\theta=\pi/2$), and along the central line ($x=0$, $y<0$, $\theta=\pi/2$). In the first case, substituting Eq. (55) into Eq. (35) at $\theta=\pi/2$, we obtain after integration over E:

$$\frac{x-a}{L_\perp}=\frac{E_0}{E\ln^{1/2}(E/E_0)}-\frac{\sqrt{\pi}}{n}\mathrm{erfc}\left[\ln^{1/2}\left(\frac{E}{E_0}\right)\right], \tag{64}$$

$$L_\perp=\sqrt{2}h_0n^{1/4}/J_0=an/\sqrt{\pi}. \tag{65}$$

For $n\gg 1$, the last term in Eq. (64) [proportional to the error function $\mathrm{erfc}(x)$] can be neglected. As shown in Appendix C, Eq. (64) is valid everywhere, except the very narrow vicinity of the defect edge $x-a<a\sqrt{n}\exp(-n/8)$, where $E\to\infty$. In this region we can retain only one term, $k=1$, with the smallest exponent $|q_{2k-1}^-|+1/n$ in the exact expansion (62). For $n\gg 1$, this yields

$$E(x,0)\approx\frac{E_0x_\pm}{|x-a|}, \quad J(x,0)=J_0\left(\frac{x_\pm}{|x-a|}\right)^{1/n}, \tag{66}$$

where $x_+=|C_1|/J_0=4a\sqrt{n}/\pi$ for $x>a$, and $x_-=|C_1|/nJ_0=4a/\pi\sqrt{n}$ for $x<a$. Thus the nonlinearity of $E(J)$ strongly

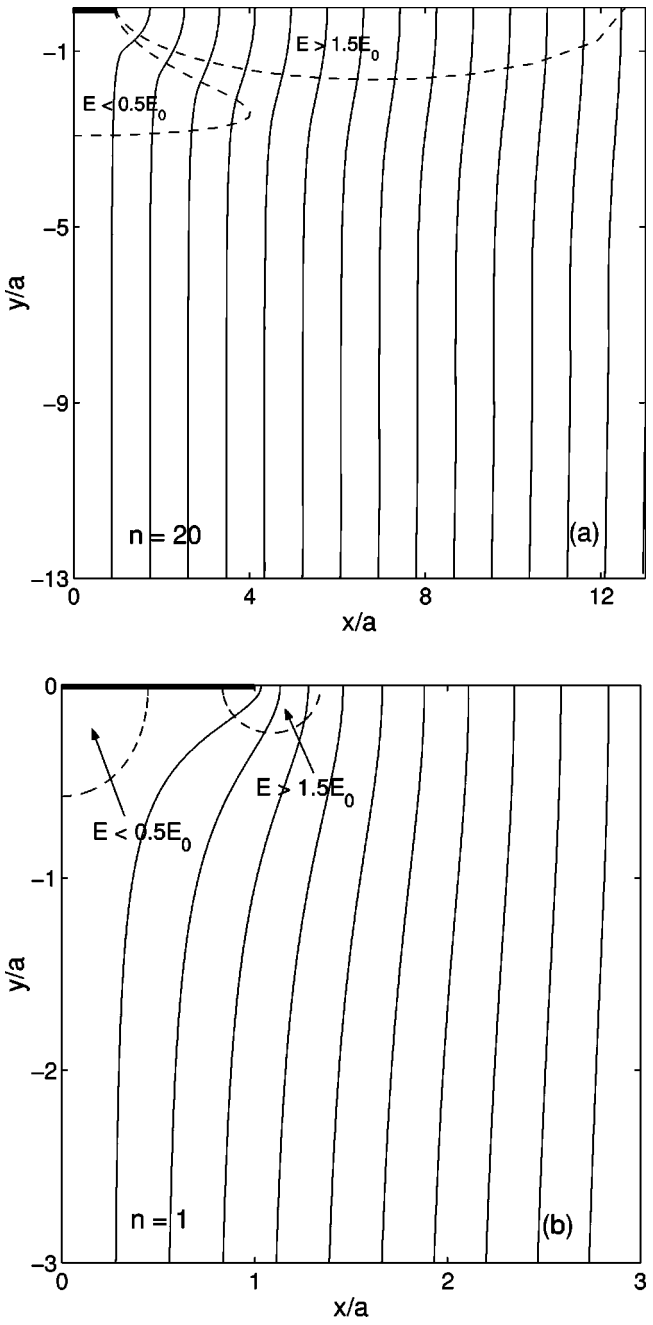

FIG. 11. Current flow around a planar defect (only one quadrant is shown). (a) corresponds to a superconductor described by Eqs. (59)–(63), where dashed contours show extended regions of enhanced ($E>1.5E_0$) and reduced ($E<E_0/2$) electric field. (b) shows current flow around the planar defect in Ohmic conductors, where perturbations of $J(x,y)$ and $E(x,y)$ decay on the length $\sim a$.

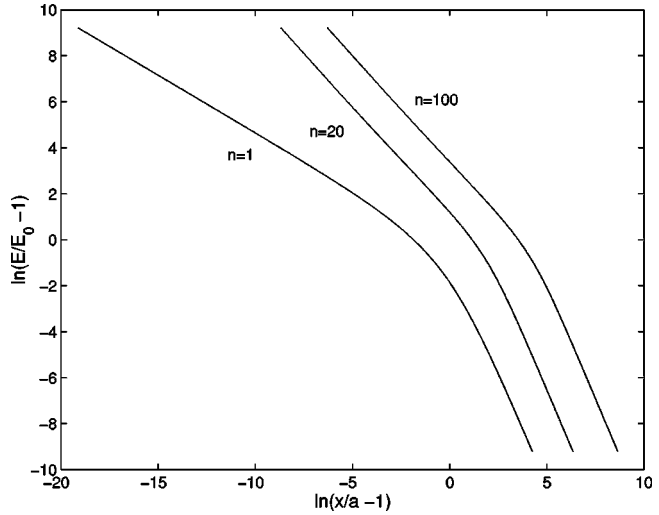

FIG. 12. Distributions of $E_y(x)$ in the plane of the defect ($y=0$), described by Eq. (64) for $n\gg 1$, and by Eq. (67) for $n=1$. For $x-a\ll a$, the curves have the slopes -1 for $n\gg 1$ and $-1/2$ for $n=1$, because near the edge of the defect, $E\propto|x-a|^{-1}$ and $E\propto|x-a|^{-1/2}$ for superconductors and normal metals, respectively. The kink in $\ln(E/E_0-1)$ at $E\sim E_0$ corresponds to a crossover to the large-x asymptotics: $E-E_0\sim nE_0(a/x)^2$ at $x\sim L_\perp$.

suppresses the singularity in $J(x)$, while enhancing the singularity in $E(x)$ at $x=a$, as compared to the Ohmic case, for which[24]

$$E(x,0)=\frac{E_0 x}{\sqrt{x^2-a^2}},\quad n=1,\ x>a. \tag{67}$$

Several important results follow from Eqs. (64) and (65), as shown in Fig. 12. First, the nonlinearity of $E(J)$ considerably enhances a characteristic magnitude E_m of the electric field. Since $E\sim anE_0/(x-a)$ over a wide region, $x<L_\perp$, near defect, we have

$$E_m\sim nE_0\gg E_0,\quad L_\perp\sim na\gg a. \tag{68}$$

Equation (64) predicts a rather slow hyperbolic dependence of $E(x,0)$ with no definite length scales, so the estimate (68) only gives a characteristic mean value of $E(x,0)$ in the region $x\sim L_\perp$, where $E_m\gg E_0$. Here $L_\perp$ quantifies a distance from the defect where $E(x,0)\simeq anE_0/x$ becomes of the order of the background electric field E_0. For larger distances, $x>L_\perp$, the parabolic dependence $E(x,0)\propto 1/(x-a)$ gradually turns into a more rapid decay, $E(x,0)-E_0\sim(an/x)^2E_0$ for $x\gg L_\perp$ (Fig. 12).

Distributions of $E(0,y)$ and $J(0,y)$ along the central line ($x=0$) are also strongly affected by the nonlinearity (Fig. 13). To calculate $E(y)$, we set $\theta=\pi/2$ in Eq. (61) and obtain

$$|y|=y_0\sum_{k=1}^{\infty}\frac{k\sqrt{\alpha_{2k}-\beta}}{\alpha_{2k}(\alpha_{2k}-\beta-n^{-1/2})}\left(\frac{E}{E_0}\right)^{\alpha_{2k}-\beta/\sqrt{n}-1/n}, \tag{69}$$

where $y_0=2^{5/2}h_0/\sqrt{\pi n}J_0=4an^{1/4}/\pi$. The dependence $E(0,y)$ for $n\gg 1$ is rather different from that for Ohmic conductors,

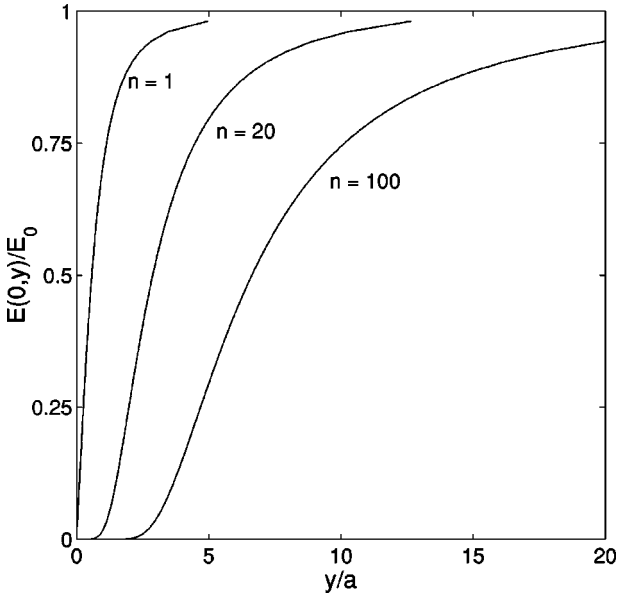

FIG. 13. Distribution of $E(y)$ along the central line, $x=0$, described by Eq. (69) for $n\gg 1$ and by Eq. (70) for $n=1$. The length $L_\parallel$ of a region of suppressed $E(y)$ scales as $a\sqrt{n}$.

$$E(0,y)=\frac{E_0|y|}{\sqrt{a^2+y^2}},\quad n=1. \tag{70}$$

For $n=1$, both $E(0,y)\propto|y|$ and $J(0,y)\propto|y|$ decrease linearly near the stagnation point $y=0$, restoring their background values E_0 and J_0 on the scale $y\simeq a$. By contrast, for $n\gg 1$, we observe a long-range depression of $E(0,y)$ on a scale $L_\parallel\gg a$, and a cusp in $J(0,y)$ (Figs. 13 and 14).

The behavior of $E(0,y)$ and $J(0,y)$ at $y\ll a$ can be obtained by taking the term with the minimum exponent with $k=1$ in Eq. (69), which yields for $n\gg 1$

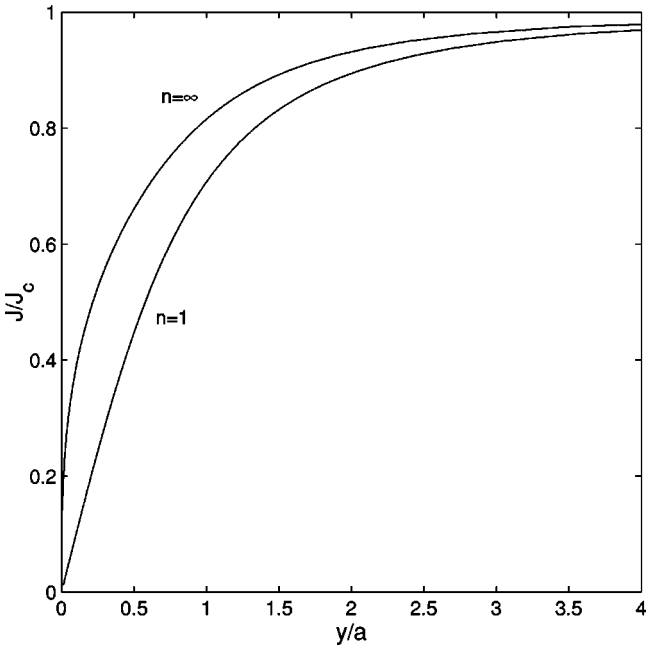

FIG. 14. Distribution of $J(y)$ along the central line, $x=0$, described by Eq. (86) for $n\to\infty$ and by Eq. (82) for $n=1$.

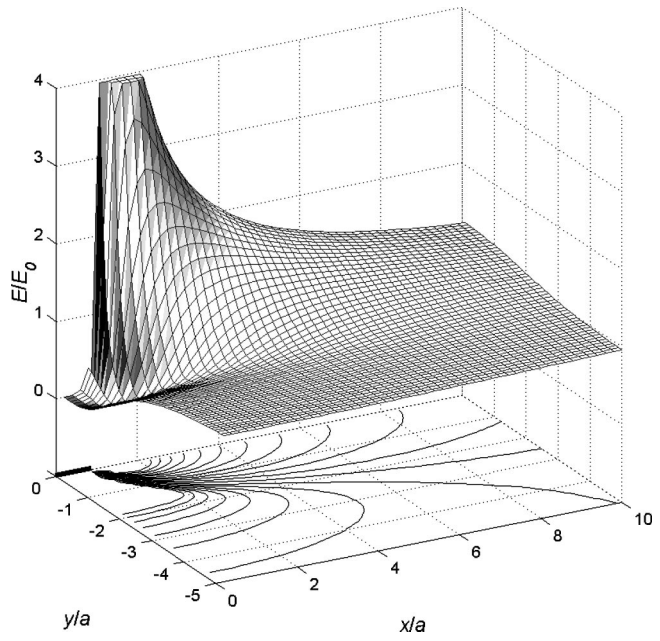

FIG. 15. Surface plot of $E(x,y)$ distribution around a planar defect for $n=20$. Shown also are the contours of constant E on the xy plane.

$$J(0,y)\propto|y|^{1/3},\quad E(0,y)\propto|y|^{n/3}. \tag{71}$$

For $n\gg1$, the electric field becomes exponentially small in a wide ''shadow'' region $y\sim a\sqrt{n}$ near the defect. For $n\gg1$, the length scale of variation of $E(0,y)$ can be obtained by replacing the summation in Eq. (69) by integration, which results in (see Appendix C)

$$E(0,y)=E_0\exp\left(-\frac{L_\parallel^2}{y^2}\right),\quad L_\parallel=a\sqrt{\frac{n}{\pi}}. \tag{72}$$

This formula gives a good approximation of the exact Eq. (69) for $x>L_\parallel$ (better than 1% for $n>20$). It follows from Eq. (72) that a characteristic length scale $L_\parallel$ of $E(0,y)$ becomes much greater than a for $n\gg1$. For $y\gg L_\parallel$, the electric field $E(0,y)$ approaches E_0 as $E(0,y)-E_0\simeq n(a/y)^2E_0$. Notice that the ratio $L_\perp/L_\parallel=\sqrt{n}\gg1$ is in agreement with the general result (16). Although Eq. (72) well describes $E(y)$ for $y>L_\parallel$, it becomes invalid for $y<L_\parallel$, where the exponential decrease of $E(y)$ given by Eq. (72) is very different from the exact result $E\propto|y|^{n/3}$. Most clearly, this difference manifests itself in current density distributions for $y<L_\parallel$: instead of the exponential decrease $J(y)\propto\exp(-a^2/\pi y^2)$ given by Eq. (72), the exact $J(y)$ exhibits a characteristic cusp of the form $J(y)\propto|y|^{1/3}$ (see Fig. 14).

Shown in Fig. 15 is the spatial distribution of the modulus $E(x,y)$, which reveals characteristic scales of the electric-field variation in all directions. The surface plot of $E(x,y)$ also gives a good approximation for the spatial distribution of local dissipation $Q=JE$ near defect for $n\gg1$. In this case variations of $J(x,y)$ are week, thus $Q(x,y)=J_0E(x,y)$ to a very good accuracy. The strong, long-range disturbance of $E(x,y)$ near the defect results in a significant excess dissipation, as will be shown below.

A. Local flux flow near sharp edges

The above solutions, obtained for the power-law $E(J)$, exhibit singularities of the electric field $E(x)\propto1/(x-a)$ near the edges of planar defects. Such a strong enhancement of $E(x)$ indicates that local flux flow can be induced near the edges, even though the E_0 away from the defect is much smaller than the crossover electric field E_c between flux flow and flux creep regimes. Description of the current flow near the edges requires accounting for the full nonlinear dependence $E(J)$.

First we consider current flow near a half infinite cut, for which the solution of the hodograph Eq. (21) should satisfy the boundary conditions $\psi(E,0)=\psi(E,\pi)=0$. This solution of Eq. (21) has the following simple form, valid for any $E(J)$:

$$\psi=\frac{A}{E}\sin\theta, \tag{73}$$

where the constant A will be obtained below. To calculate $z(E,\theta)$, we substitute Eq. (73) into Eq. (34) and integrate over θ, which yields

$$z=-\frac{A}{2EJ}e^{2i\theta}+f(E). \tag{74}$$

Here $f(E)$ is a real function of E [the imaginary part vanishes because of the boundary condition $y(E,0)=y(E,\pi)=0$]. The equation for f can be obtained by substituting Eqs. (73) and (74) into Eq. (19):

$$\partial_E f=\frac{A}{2}\left(\frac{\sigma}{J^2E}-\frac{1}{JE^2}\right). \tag{75}$$

The boundary condition for $f(E)$ follows from the fact that the electric field $E(x,y)$ becomes infinite at the end of the cut ($x=y=0$), as shown in Fig. 6. Then Eq. (74) gives $f(\infty)=0$, and integration of Eq. (75) yields

$$f(E)=A\left(\int_E^\infty\frac{dE'}{JE'^2}-\frac{1}{2JE}\right). \tag{76}$$

Equations (73), (74), and (76) give a solution of the nonlinear Maxwell equations, which describe current flow around the half infinite cut for arbitrary $J(E)$. This solution also describes approximately the current flow near the edge of a cut of finite length $2a$, where the scaling constant A is determined by the current flow on the length of order a away from the edges.

To calculate A we need to match Eq. (73) with the solution of the previous section, which describes current flow around a cut of length $2a$, for the power law $J(E)$. To do so we note that for $E\ll E_c$, the power-law approximation is valid everywhere around the cut, except small regions near the ends. Here $E\gg E_0$, so the main contribution to ψ comes from the term with $k=1$ and minimum $|q_k^-|$ in Eq. (60). This yields the same universal dependence $\psi(E,\theta)=C_1(E_0/E)\sin\theta$ as Eq. (73), whence $A=C_1E_0$. Using Eqs. (58) and (63), we obtain for $n\gg1$

$$A=\frac{2^{5/2}h_0 n^{3/4}E_0}{\sqrt{\pi}(n+1)}=\frac{4\sqrt{n}}{\pi}aJ_0E_0. \tag{77}$$

Separating real and imaginary parts of Eq. (74), we get

$$x-f(E)=-\frac{A}{2JE}\cos 2\theta, \tag{78}$$

$$y=-\frac{A}{2JE}\sin 2\theta. \tag{79}$$

Thus the contours of constant E are circles of radius $A/2JE$ centered at $x=f(E)$, $y=0$ (Fig. 6). Equation (78) and (79) describe the intermediate asymptotics of the current distribution in a small region of radius $R\ll a$ near the edge (see below). Away from the edge, Eqs. (78) and (79) merge with the solution of the previous section, which describes the current flow around the cut and provides the correct asymptotics $E\to E_0$ at infinity.

We can further simplify Eq. (76), using the fact that $J(E)$ in superconductors varies rather weakly, even for significant (by several orders of magnitude) changes of E (see Fig. 1). Since the main contribution to the integral in Eq. (76) comes from $E'\simeq E$, we can therefore take the slowly varying function $J(E')\approx J(E)$ out of the integral and obtain

$$f=A/2JE. \tag{80}$$

To calculate corrections to $f(E)$ due to flux flow, we assume that $J(E)=J_c+\sigma_f E$ for $E>E_c$, where σ_f is the flux flow conductivity. Then the integration of Eq. (76) gives $f\cong A/2J_cE+A\sigma_f/2J_c^2$, if $\sigma_f E/J_c\ll 1$.

The radius R of the circular flux flow region near the edge $[E(x,y)>E_c]$ can be obtained by setting $E=E_c$ in Eqs. (78) and (79) and substituting there Eqs. (77) and (80):

$$R=\frac{A}{2J_cE_c}=\frac{2a\sqrt{n}}{\pi}\left(\frac{E_0}{E_c}\right). \tag{81}$$

Excluding θ from Eqs. (78)–(80), we obtain the electric-field distribution near the edge:

$$E(x,y)=\frac{4a\sqrt{n}xE_0}{\pi(x^2+y^2)},\quad x>0. \tag{82}$$

The above matching of two solutions near the edge and around the strip is justified, if the radius of the flux flow region R is small compared to the length of the strip $2a$. From Eq. (81) we find that $R\ll a$ if $E_0\ll E_c/\sqrt{n}$. This condition indicates that because of the enhancement of the electric field near the edges, the local flux flow occurs when the bulk E_0 is much smaller than the crossover field E_c. However, there is a much stronger applicability condition of the above description, based on the one-term approximation of the sum in Eq. (62). As shown in Appendix C, the terms with $k>1$ in Eq. (62) can be neglected, if $E_0\ll E_f\sim E_c\exp(-n/8)$. For $E_0\gg E_f$, the flux flow region near the edge becomes noncircular, being essentially stretched out along the x axis [Fig. 11(a)]. An analysis of this case given in Appendix C, shows that as E_0 increases, the size of the flux flow region along the x axis, $L_\perp$, turns out to be much larger than its size, $L_\parallel$, along the y axis:

$$L_\perp\sim anE_0/E_c,\quad L_\parallel\sim a\sqrt{n}E_0/E_c. \tag{83}$$

The condition that the flux flow region is much smaller than a now requires $E_0\ll E_c/n$.

B. Critical state limit, $n\to\infty$

The hodograph method enables us to trace the evolution of current flow with n and see what happens in the critical state limit, $n\to\infty$. Because of the ambiguity of the Bean model discussed in the Introduction, current flow in the true critical state should be first calculated for large, but finite n values and only then the limit $n\to\infty$ is to be taken. We consider this rather nontrivial limit in detail for current flow past a planar defect, assuming that $J_0=J_c$ at infinity. As was shown before, the solution for $J(x,y)$ describes two regions of current flow, corresponding to $J<J_c$ and $J>J_c$. The solutions for $J<J_c$ can be obtained from Eqs. (61) straightforwardly, by taking the limit $n\to\infty$. However, the solutions with $J>J_c$ should be handled with care, since in the Bean model, current densities $J=J_c+0$ correspond to infinite E.

For $J<J_c$, and $n\to\infty$, the stream function ψ described by Eq. (61) can be presented in the following form independent of n:

$$\psi=\frac{8aJ_c}{\pi}\sum_{k=1}^{\infty}(-1)^k k\left(\frac{J}{J_c}\right)^{4k^2}\sin 2k\theta, \tag{84}$$

$$z=-\frac{16a}{\pi}e^{i\theta}\sum_{k=1}^{\infty}\frac{(-1)^k k^2}{4k^2-1}\left(\frac{J}{J_c}\right)^{4k^2-1}\times(\cos 2k\theta-2ik\sin 2k\theta). \tag{85}$$

The sums in Eqs. (84) and (85) can be expressed in terms of elliptical theta functions.[37] The asymptotics of $\mathbf{J}(x,y)$ considerably simplify far away from the defect, ($|z|\gg a$), as shown in Appendix D.

From Eqs. (85), we obtain the current distribution $J(y)$ along the central line $x=0$, $\theta=\pi/2$,

$$|y|=\frac{16a}{\pi}\sum_{k=1}^{\infty}\frac{k^2}{4k^2-1}\left(\frac{J}{J_c}\right)^{4k^2-1}, \tag{86}$$

which is shown in Fig. 14. Near the stagnation point, $y\to 0$, the function $J(y)\simeq J_c(3\pi y/16a)^{1/3}$ exhibits a cusp. Notice that $J(y)$ restores the bulk value J_c on the length $\sim a$, unlike the electric field $E(y)$, which varies on the scale $\sim a\sqrt{n}$.

The limit $n\to\infty$ cannot be directly taken in the region $J>J_c$, since the sum in Eq. (62) diverges. So we first consider the well-behaved case of large, but finite, n and calculate the boundary between the regions of current flow with $E>E_0$ and $E<E_0$ in the real space [see Fig. 16(a)]. As shown in Appendix D, the boundary is given by the curve $y(x)$, which for $n\gg 1$ is described parametrically as follows:

$$x-a=h_0\frac{e^{-\beta\gamma}}{\sqrt{\gamma}}, \tag{87}$$

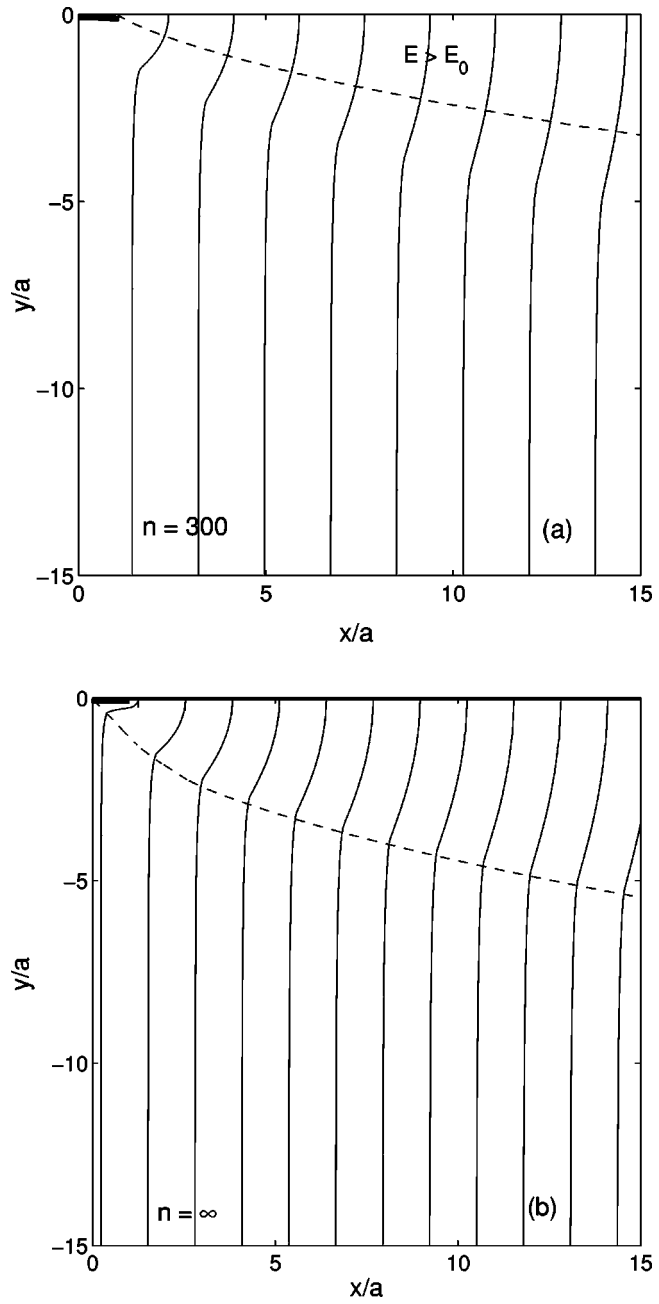

FIG. 16. Current flow around the planar defect for large (a) and infinite (b) n values, described by Eqs. (59)–(63) and Eqs. (84) and (85), respectively. The dashed line in Fig. 16(a) shows the boundary between the regions of current flow with $E>E_0$ and $E<E_0$. In the limit $n\to\infty$, this boundary reduces to a ray, $y=0$, shown in (b). The dashed line in (b) shows the d line, which is well described by the parabolic function (89) for $x>2a$.

$$|y|=h_0\left(\frac{1}{\sqrt{n\gamma}}+\sqrt{\gamma}\right)e^{-\beta\gamma}, \tag{88}$$

where $\gamma=\pi/2-\theta$. From Eqs. (87) and (88), we obtain that $|y|\simeq(x-a)/\sqrt{n}$ far away from the defect. In the limit $n\to\infty$, the whole region of $E>E_0$ reduces to a ray along the x axis, where the electric field formally diverges. The voltage across this region, $V_0\sim E(x)\Delta y$, is of order $E_0a\sqrt{n}$, since $E(x)\sim E_0an/(x-a)$, and $\Delta y\sim(x-a)/\sqrt{n}$. In the limit $n\to\infty$, we should take $J_0=J_c-0$, so that the voltage across the singular line $V_0\sim a\sqrt{n}E_c(J_0/J_c)^n$, vanishes. Thus we may ignore the region $E>E_0$, and Eqs. (84) and (85) give a complete description of the current distribution in the true critical state, $E=0$. Shown in Fig. 16(b) are the current streamlines given by Eqs. (84), which are practically indistinguishable from those for large but finite n values in Figs. 11(a) and 16(a). However, the dc electric field distribution for large but finite n remains very different from the critical state predictions. Indeed, instead of converging to a straight line along the x axes, the region of $E>E_0$ in Fig. 16(b) significantly extends along the direction of current flow even for $n=300$, which is much larger than typical values of $n\sim10$–50 for superconductors.

In the limit, $n\to\infty$, current flow around the defect has the singular d lines, which come out of the stagnation points and extend to infinity as shown in Fig. 16(b). Near the stagnation point the d lines make a 45° angle with the x axis and have the same structure as for current flow near the corner, described by Eq. (50). For ($|z|\gg a$), the following simple equation of the d line can be obtained, as shown in Appendix D:

$$x=y^2/y_\infty, \tag{89}$$

where $y_\infty=8a/\sqrt{2\pi e}\approx1.94a$. Therefore, far away from the planar defect, the d lines become parabolic, whereas the current streamlines between the d lines in Fig. 15(b) are approximately circular, to the accuracy of slowly varying logarithmic factors (see Appendix D). These results are qualitatively similar to current flow around the cylindrical void in the Bean model (Fig. 4). However, unlike Bean's d line in Fig. 4, current flow near the d lines described by exact Eqs. (85) exhibits no discontinuity in the tangential component of $\mathbf{J}$, thus satisfying the condition $\nabla\times\mathbf{E}=0$, even in the limit $n\to\infty$.

VI. DISSIPATION NEAR PLANAR DEFECTS

In this section we obtain a general expression for the excess total dissipation Q due to defects:

$$Q=\int dx\,dy(JE-J_0E_0), \tag{90}$$

where the term J_0E_0 corresponds to a uniform sample without defects. Now we transform from integration over x and y to the hodograph variables, E and θ, and obtain (see Appendix E)

$$Q=\int_0^{2\pi}d\theta\int_0^\infty(EJ-E_0J_0)\left[E(\partial_E\psi)^2+\frac{\sigma}{J}(\partial_\theta\psi)^2\right]\frac{dE}{J^2}. \tag{91}$$

Substituting Eq. (28) into Eq. (91) and integrating over θ from 0 to 2π, we present Q in the form

$$Q=\pi\sum_m C_m^2\int_0^\infty(JE-J_0E_0)\left[E(\partial_Ef_m)^2+\frac{\sigma m^2}{J}f_m^2\right]\frac{dE}{J^2}. \tag{92}$$

Here integration from 0 to 2π implies that current flow contains all possible orientations of J, as it occurs for a planar defect in an infinite superconductor.

We apply these formulas to calculate dissipation power Q, caused by planar defects. We first consider a simpler case of a semi-infinite cut in Fig. 6 and calculate the total dissipation power ΔQ inside a circular region at the edge where E exceeds a certain electric-field threshold, E_c. Substituting Eq. (73) into Eq. (91), we first integrate over θ from 0 to π (as seen from Fig. 6, the current flow around a semi-infinite, unlike planar defects of finite length, is represented by only half of the hodograph plane, $0<\theta<\pi$). Integrating then over E, as explained in Appendix E, we obtain a simple exact result,

$$\Delta Q=\pi A^2/2J_cE_c, \tag{93}$$

valid for any J-E relation. For instance, if E_c is chosen in the flux creep region, ΔQ is unaffected by the flux flow portion of $E(J)$.

Now we calculate Q for a planar defect of length $2a$ for the power-law $E(J)$ characteristic. Substituting Eq. (23) into Eq. (91) and integrating over E, we obtain

$$Q=\frac{\pi E_0}{2J_0}(n+1)\sum_{m=1}^{\infty}\left[\frac{|q_{2m-1}^-|C_{2m-1}^2}{n|q_{2m-1}^-|+1}-\frac{q_{2m}^+C_{2m}^2}{nq_{2m}^+-1}\right], \tag{94}$$

where the subscripts $+$ and $-$ corresponds to the signs in front of the square root in Eq. (32). The positive terms, proportional to C_{2m-1}^2 in Eq. (94), represent an excess dissipation due to enhanced electric field around a defect, while the negative terms, proportional to C_{2m}^2, account for reduced dissipation in the stagnation regions. For Ohmic conductors, these two opposite contributions exactly cancel each other, giving $Q=0$ for $n=1$ (see Appendix E). For $n\gg1$, the spatial distribution of Joule dissipation JE is similar to $E(x,y)$ shown in Fig. 15. In this case, there appears an excess dissipation ($Q>0$), since the contribution to Q from the electric-field enhancement along the x axis (on the scale $L_\perp\sim na$) is much greater than the negative contribution of the stagnation regions (on the scale $L_\parallel\sim\sqrt{n}a$). Substituting Eqs. (58) for C_m, into Eq. (94) and evaluating the sum as explained in Appendix E, we obtain

$$Q=J_0E_0a^2(n-1)\sqrt{n}. \tag{95}$$

For $n\gg1$, Eq. (95) is an exact asymptotics of $Q(n)$, which approximates Eq. (94) to an accuracy better than 1% for $n>10$ and 6% for $5<n<10$. The physical meaning of Eq. (95) becomes more transparent, by presenting Q in the form $Q\simeq\pi L_\parallel J_0\int_a^\infty(E-E_0)dx$, which is just the excess dissipation in the region of substantial enhancement of $\mathbf{E}(\mathbf{r})$ by the defect. Using Eqs. (64) and (65) for $E(x)$, we obtain $Q\sim\pi J_0E_0L_\parallel L_\perp$, which gives the correct leading term, $Q\simeq E_0J_0a^2n^{3/2}$.

VII. DISCUSSION

The analytical results obtained in this paper reveal essential features of nonlinear 2D current flow, which can affect the current-carrying capability and macroscopic electrodynamics of superconductors. This influence mostly results from the fact that planar obstacles cause strong enhancement and long-range decay of electric-field disturbances. These effects are important for applications, in particular, ac losses, critical state stability, and current flow in thin-film superconducting circuits. The use of the hodograph technique enabled us to address such characteristics of nonlinear current flow, as orientational current flow domains and the structure of current domain walls. In addition, we were able to trace the evolution of current distributions with n and a nonanalytic crossover to the critical state limit, $n\to\infty$, when singular d lines emerge.

The fact that a planar obstacle of size a greatly enhances electric-field disturbances over scales $L_\perp\sim an$ perpendicular to current flow or $L_\parallel\sim a\sqrt{n}$ along current flow results in long-range interaction between defects, and strong effect of the sample geometry. Indeed, even a sparse network of planar defects can substantially reduce the effective current-carrying cross section, if the mean spacing between the defects is smaller than $L\sim an$. For typical values of $n\sim30$, such a nonlinear blockage of transport current by defects can occur at rather small concentration of obstacles, which occupy only few percent of the geometrical cross section of a superconductor. This effect can have important implications for current percolation through arrays of planar defects, such as grain boundaries in HTS polyscrystals (Fig. 2). It also contributes to multiple current-limiting mechanisms in HTS conductors, such as Bi tapes and biaxially textured $YBa_2Cu_3O_7$ coated conductors.[38] For instance, a microcrack, in a film of thickness d (Fig. 3), can cause a strong local peak of $E(x)$ in YBCO coated conductor, even for rather small defects $a>d/n\ll1$. In turn, such local peaks of voltage and dissipation change the global current-voltage characteristic of the whole conductor, similar to the effect of macroscopic random inhomogeneities.[12] A detailed analysis of the significant finite-size effects for current flow in restricted geometries shown in Fig. 3 will be given elsewhere.[25]

The features of nonlinear current flow discussed above can be observed by the magneto-optical (MO) technique, which indeed revealed long-range disturbances of the normal component of $\mathbf{H}(x,y)$ around macroscopic defects in HTS's.[7,9] For instance, characteristic flamelike shapes of the magnetic-flux disturbances around defects on MO images are similar to the contours of constant E shown in Figs. 11 and 15. By measuring the scales $L_\perp$ and $L_\parallel$ of magnetic-flux disturbance, one can extract both the n value, $n\simeq(L_\perp/L_\parallel)^2$, and the size of the defect, $a\sim L_\perp/n$, even if the defect is smaller than the MO resolution (usually $\simeq50$–10 μm). Extensive stagnation regions ($L_\parallel\sim a\sqrt{n}$) of exponentially small electric field constitute another feature of nonlinear current flow around planar defects [Fig. 11(a)] which could be observed in MO experiments. This nonlinear ''shadow effect'' manifests itself in the distribution of flux velocities, $\mathbf{v}=[\mathbf{H_0}\times\mathbf{E}]/H_0^2$, in a strong magnetic field H_0 when vortices move along equipotential lines, $\varphi(x,y)=$const. Vortex velocity $\mathbf{v}$ sharply increases in the regions of enhanced electric field near the edges of the planar defect, which thus becomes a flow channel for magnetic flux [see Figs. 11(a) and 15]. These flux jets are sandwiched between two macroscopic stagnation regions of nearly motionless flux which result from the geometry of the current flow and the strong nonlinearity of $E(J)$, but are not due to enhanced flux pinning.

The excess dissipation Q caused by defects is another important feature of the strong nonlinearity of $E(J)$. Superconducting materials, and especially HTS's, contain many macroscopic current-limiting defects (microcracks and high-angle grain boundaries),[6] which contribute significantly to the overall ac losses and dissipation. As an example, we consider a sparse array of planar defects of size $\sim a$ spaced by $l \gg a$. Then we obtain from Eq. (95) that the defects result in the excess dissipation power $\sim n^{3/2}(a/l)^2 J_0 E_0$ per unit volume, which becomes of the order of the background bulk dissipation power $J_0 E_0$, if $l < a n^{3/4}$. Therefore the overall dissipation will be dominated by defects, if they occupy a rather small fraction $\sim n^{-3/4}$ of the geometrical cross section of the sample (few percent for the typical n values ~ 20–30 for superconductors). The excess dissipation due to defects can also trigger local thermal instabilities in high-J_c superconductors.[36] Such instabilities develop mostly in the regions of enhanced heat generation $E > E_0$ in Figs. 11(a) and 15, which dominate the overall Q. Another type of orientational current instabilities can be caused by the high anisotropy of HTS's,[21] when current is forced to flow along the c axis by microcracks[8] or a ''brick-wall'' structure of in-plane tilt grain boundaries.[39]

ACKNOWLEDGMENTS

We are grateful to D. C. Larbalestier and A. P. Malozemoff for discussions. This work was supported by the NSF MRSEC (Grant No. DMR 9214707) and EPRI.

APPENDIX A: ANALYTIC PROPERTIES OF THE COMPLEX POTENTIAL

2D current flow in Ohmic conductors is described by the complex potential

$$w(z) = \varphi - i\rho\psi, \tag{A1}$$

which is an analytic function of $z = x + iy$. The analyticity of $w(z)$ greatly simplifies the calculation of 2D current distributions, allowing exact solutions for the geometries shown in Fig. 3 to be obtained using conformal mapping.[32] The condition that $w(z)$ is an analytic function can be written in the form

$$\frac{dw}{d\bar{z}} = 0, \tag{A2}$$

where the bar denotes complex conjugate, and the complex differentiation of any function $f(z) = u + iv$ is defined as[34]

$$\frac{df}{d\bar{z}} = \frac{1}{2}\left(\frac{\partial u}{\partial x} - \frac{\partial v}{\partial y}\right) + \frac{i}{2}\left(\frac{\partial v}{\partial x} + \frac{\partial u}{\partial y}\right). \tag{A3}$$

The fact that $df/d\bar{z} = 0$ for any analytic function $f(z)$ follows from the Cauchy-Riemann conditions, $\partial_x u = \partial_y v$, $\partial_y u = -\partial_x v$. The electric-field distribution, $E_x + iE_y = E\exp(i\theta)$, can be calculated from

$$E e^{-i\theta} = -\frac{dw}{dz}. \tag{A4}$$

Another feature of Ohmic conductors is that the complex potential $w(u)$ is also an analytic function in the hodograph plane, $u = \eta - i\theta$, where $\eta = \ln(E/E_0)$.

In nonlinear conductors, ρ depends on E, so neither $w(z)$ nor $w(u)$ are analytic functions. We consider properties of w for the power law $E(J)$, for which Eqs. (20) can be written in the following symmetric form:

$$\partial_\eta \varphi = (\rho_0/\sqrt{n}) e^{2\beta\eta} \partial_\theta \psi, \tag{A5}$$

$$\partial_\theta \varphi = -(\rho_0/\sqrt{n}) e^{2\beta\eta} \partial_\eta \psi, \tag{A6}$$

where $\beta = (n-1)/2\sqrt{n}$, $\eta = n^{-1/2}\ln(E/E_0)$, and $\rho_0 = E_0/J_0$. Defining new functions, $h_1 = \varphi\exp(-\beta\eta)$ and $h_2 = (\sqrt{n}/\rho_0)\psi\exp(\beta\eta)$, we present Eqs. (A5) and (A6) in the form

$$\partial_\eta h_1 - \partial_\theta h_2 = -\beta h_1, \tag{A7}$$

$$\partial_\theta h_1 + \partial_\eta h_1 = \beta h_2. \tag{A8}$$

These equations can be combined into a single complex equation for the effective complex potential, $w_0 = h_1 - ih_2$. Using complex differentiation (A3) with respect to $u = \eta - i\theta$, we obtain the equation for w_0 in the form of a first-order Carleman equation,

$$\frac{dw_0}{d\bar{u}} = -\frac{\beta}{2}\bar{w}_0, \tag{A9}$$

which describes generalized analytic functions.[33] Therefore calculations of current flow in nonlinear conductors can be formulated in terms of generalized analytic functions for the effective potential $w_0(u)$ in the hodograph plane, $u = \eta - i\theta$. This fact enables one to calculate 2D nonlinear current flow by constructing an appropriate generalized analytical function,[22] using methods which have been developed in the literature.[33] Expressing w_0 in terms of φ and ψ, we obtain

$$w_0 = \varphi e^{-\beta\eta} - \frac{i\rho_0}{\sqrt{n}} e^{\beta\eta}\psi. \tag{A10}$$

For $n = 1$, the effective potential w_0 reduces to w.

APPENDIX B: NORMALIZATION CONSTANT

To calculate h_0, we equate Eqs. (61) and (62) to obtain the self-consistency condition $z(+0,0) = z(-0,0)$, whence

$$a = -\frac{1}{J_0\sqrt{n}} \sum_{k=1}^{\infty} \left(\frac{2k}{u_k} C_{2k} + \frac{2k-1}{p_k} C_{2k-1}\right). \tag{B1}$$

It is convenient to write Eq. (B1) as $h_0 = -aJ_0/I$, where I is obtained from Eqs. (57) and (58) in the form

$$I = \frac{2^{3/2}}{\sqrt{\pi n}} \sum_{m=1}^{\infty} \left[\frac{2m(-1)^m\sqrt{\alpha_{2m}-\beta}}{(4m^2-1)\alpha_{2m}}\left(\alpha_{2m} + \beta + \frac{1}{\sqrt{n}}\right) + \frac{(2m-1)(-1)^m\sqrt{\alpha_{2m-1}+\beta}}{\alpha_{2m-1}(\alpha_{2m-1}+\beta+1/\sqrt{n})}\right]. \tag{B2}$$

For $n \gg 1$, this sum is dominated by the first term in the square brackets, where $1/\sqrt{n}$ in $(\alpha_{2m}+\beta+1/\sqrt{n})$ can be neglected. Then I reduces to

$$I=\frac{2^{3/2}}{\sqrt{\pi n}}\sum_{m=1}^{\infty}(-1)^m\left(\frac{\sqrt{\alpha_{2m}+\beta}}{(4m^2-1)\alpha_{2m}}+\frac{\sqrt{\alpha_{2m}+\beta}}{\alpha_{2m}}\right). \tag{B3}$$

The first part of this sum, I_1, is rapidly converging over $m \sim 1$, so the slowly varying factor $\sqrt{\alpha_{2m}+\beta}/\alpha_{2m}$ can be replaced by its constant value at $m=1$. Then the summation yields

$$I_1=-\frac{\pi-2}{\sqrt{\pi n\beta}}. \tag{B4}$$

The second part of I is an expression of the form $I_2=\Sigma_{m=1}^{\infty}(-1)^m F_m$, where F_m, given by the second term in the square brackets, decreases slowly with m for $n \gg 1$. To turn I_2 into a rapidly converging series, we write

$$I_2=\sum_{m=1}^{\infty}(F_{2m}-F_{2m-1})=\sum_{m=1}^{\infty}\sum_{k=1}^{\infty}\frac{1}{2^k k!}\frac{d^k F_{2m}}{dm^k}, \tag{B5}$$

where F_m is nearly constant for $m<\beta$, and decreases as $1/\sqrt{m}$ for $m>\beta$. Therefore each differentiation of F_m over m brings a small factor $\sim 1/\sqrt{n}$, so the main contribution to I_2 comes from the term with $k=1$. Since dF_m/dm is a slow function of m, we can replace summation in Eq. (B5) by integration using the Poisson-Euler formula[34] written in the form

$$\sum_{m=1}^{\infty}f(m)\approx\int_0^{\infty}f(x)dx-\frac{f(0)}{2}-\frac{\partial_m f(0)}{12}, \tag{B6}$$

where $f_m=0.5dF_m/dm$. Since F_m is a function of m^2, the second term in the right-hand side of Eq. (B6) vanishes, and the last term $\sim\beta^{-5/4}\ll 1$ is negligible. As a result, the sum (B6) equals $-F_0/2$, thus

$$I_2=-\frac{2}{\sqrt{\pi n\beta}}. \tag{B7}$$

Combining I_1 and I_2, we obtain Eq. (63), which approximates Eq. (B1) to the accuracy better than 1% for $n>5$.

APPENDIX C: ASYMPTOTICS OF $z(E,\theta)$

To sum up Eq. (69) at $n \gg 1$, we consider the region of $x<a\sqrt{n}$, where $E \ll E_0$. The convergence of the sum is then mostly determined by the factors $(E_0/E)^{\lambda_k}$, where $\lambda_k=(\alpha_{2k}-\beta)/\sqrt{n}-1/n$. In this case the main contribution to Eq. (69) for $n \gg 1$ comes from the region $k<\beta$, where the slowly varying factor α_{2k} can be taken out of the sum at $k=1$. Then $\alpha_{2k}-\beta\approx 2k^2/\beta$, $\lambda_k\approx 4k^2/n$, and Eq. (69) reduces to

$$y=\frac{4a}{\pi}\sum_{k=1}^{\infty}\left(\frac{E}{E_0}\right)^{4k^2/n}. \tag{C1}$$

For $n \gg 1$, the sum in Eq. (C1) can be evaluated with the use of Eq. (B6), giving $[\pi n/\ln(E/E_0)]^{1/2}/4$. As a result, we arrive at Eq. (72). This approach gives the intermediate asymptotics of $E(0,y)$ at $y \sim L_{\parallel}$. The behaviors of $E(0,y)$ for $y\to\infty$ should be obtained in a different way, since for $E\to E_0$, the sum in Eq. (69) diverges. The main contribution then comes from $k \gg \beta$, and Eq. (69) becomes

$$y=\frac{a}{\pi\sqrt{2}n^{1/4}}\sum_{k=1}^{\infty}\frac{1}{\sqrt{k}}\left(\frac{E}{E_0}\right)^{2k/\sqrt{n}}. \tag{C2}$$

For $n \gg 1$, evaluation of this sum with the use of Eq. (B6), gives $y=a\sqrt{n/\pi}\ln^{-1/2}(E_0/E)$. This yields the same asymptotic behavior of $E(0,y)-E_0=E_0(L_{\parallel}/y)^2$ as Eq. (72).

To calculate the distribution of $E(x,y)$ near the edges, we write Eq. (62) in the form

$$z-a=\frac{2^{3/2}h_0e^{i\theta}}{\sqrt{\pi}J_0}\sum_{k=1}^{\infty}\frac{(-1)^k\sqrt{\alpha_{2k-1}+\beta}}{p_k\alpha_{2k-1}}\left(\frac{E_0}{E}\right)^{\sigma_k}\times\left[\frac{2k-1}{\sqrt{n}}\cos(2k-1)\theta+i(\alpha_{2k-1}+\beta)\sin(2k-1)\theta\right], \tag{C3}$$

where $\sigma_k=|q_{2k-1}|+1/n$. Near the edges, where $E \gg E_0$, the convergence of this sum is determined by the small factor $(E_0/E)^{\sigma_k}=\exp[-\sigma_k\ln(E/E_0)]$ at $(2k-1)^2<n$. There are two characteristic domains. The first one is very close to the edge $(E\to\infty)$, so that the sum (C3) is dominated by the term $k=1$, for which the exponent $\sigma_1=1+1/n$ is minimum. In this case the term with $k=2$ is negligible, that is, $\exp[-(\sigma_2-\sigma_1)\ln(E/E_0)]\ll 1$. For $n \gg 1$, we get $\sigma_2=1+9/n$, thus the sum in Eq. (C3) is determined by only one term with $k=1$, if $(8/n)\ln(E/E_0)>1$. This criterion defines the size of the region, $r_c\sim a\sqrt{n}\exp(-n/8)$, at the edge, where the one-term approximation holds.

Since r_c decreases exponentially with n, there is a wide region near the planar defect where $\ln(E/E_0)\gg 1$, but the terms with $k>1$ in Eq. (C3) cannot be neglected. In the large region $r_c \ll x \ll an$, where $E \gg E_0$, the convergence of the sum (C3) is mostly determined by the factor $(E_0/E)^{\sigma_k}$, while the much weaker k dependence of α_{2k-1} can be neglected. In this case we can replace $\alpha_{2k-1}\approx\beta$ and expand $\sigma_k\approx 1+(2k-1)^2/n$. As a result, Eq. (C3) for $n \gg 1$ reduces to

$$z-a=\frac{2^{5/2}h_0e^{i\theta}}{\sqrt{\pi}n^{1/4}J_0}\left(\frac{E_0}{E}\right)\left(\frac{I'}{n}+I\right), \tag{C4}$$

$$I(\theta,\tau)=\sum_{k=1}^{\infty}(-1)^k e^{-\tau(2k-1)^2}\sin(2k-1)\theta. \tag{C5}$$

Here $\tau=n^{-1}\ln(E/E_0)$, $I'=\partial_\theta I$, and $I(\theta,\tau)$ can be expressed in terms of elliptical theta-functions.[37] Notice that $I(\theta,\tau)$ satisfies the ''diffusion'' equation

$$\partial_\tau I=\partial_{\theta\theta}I. \tag{C6}$$

Separating real and imaginary parts of Eq. (C4), we express $x(\theta,\tau)$ and $y(\theta,\tau)$ in terms of $I(\theta,\tau)$:

$$x-a=l[(I'/n)\cos\theta-I\sin\theta], \tag{C7}$$

$$y=l[(I'/n)\sin\theta+I\cos\theta], \tag{C8}$$

where $l=(4a\sqrt{n}/\pi)(E_0/E_c)$. To calculate $I(\theta,\tau)$, we multiply Eq. (C5) by $\sin(2m-1)\theta$ and integrate from 0 to $\pi/2$:

$$\int_0^{\pi/2} I\cos(2m-1)\gamma d\gamma=\frac{\pi}{4}e^{-(2m-1)^2\tau}, \tag{C9}$$

where $\gamma=\pi/2-\theta$. We consider the wide region of E, where $\ln(E/E_0)>1$, but $\tau\ll 1$. The main contribution to the integral in Eq. (C9) then comes from $\gamma\ll 1$, so we can extend the upper integration limit to ∞ and obtain

$$I(\gamma,\tau)=\frac{\sqrt{\pi}}{4\sqrt{\tau}}e^{-\gamma^2/4\tau}. \tag{C10}$$

This is a well-known solution of the diffusion Eq. (C6), which describes the evolution of $I(\gamma,\tau)$ in an infinite 1D media after applying a pulse $\propto\delta(\gamma)\delta(\tau)$.[34]

Substituting Eq. (C10) into Eqs. (C7) and (C8) and using the fact that $\gamma\ll 1$, we obtain the distribution $\mathbf{E}(x,y)$ in the following parametric form:

$$x-a=lI,\quad y=[1+1/2\ln(E/E_0)]l\gamma I. \tag{C11}$$

Excluding γ from Eq. (C11), we obtain contours of equal $E(x,y)=E_c$:

$$|y|=g(x-a)\ln^{1/2}\frac{L_\perp}{x-a}, \tag{C12}$$

$$g=\frac{2}{\sqrt{n}}\ln^{1/2}(E_c/E_0)\left(1+\frac{1}{2\ln(E_c/E_0)}\right), \tag{C13}$$

$$L_\perp=\frac{an}{\sqrt{\pi}\ln^{1/2}(E_c/E_0)}\left(\frac{E_0}{E_c}\right). \tag{C14}$$

The contour $y(x)$ shown in Fig. 11(a) is quite different from the circular flux flow regions of the $k=1$ approximation. Here the length $L_\perp$ of the domain with $E>E_c$ along the x axis becomes much larger than its size $L_\parallel$ along the y axis. Indeed, the maximum of $y(x)=L_\parallel$ occurs at $x=L_\perp/\sqrt{e}$. Substituting this into Eq. (C12), we obtain

$$L_\parallel=a\sqrt{\frac{2n}{\pi e}}\left[1+\frac{1}{2\ln(E_c/E_0)}\right]\left(\frac{E_0}{E_c}\right). \tag{C15}$$

To the accuracy of slowly varying logarithmic terms, we again arrive at the universal relation $L_\perp\sim\sqrt{n}L_\parallel$.

APPENDIX D: CRITICAL STATE LIMIT

To calculate the boundary ($\eta=0$) between the regions $E<E_0$ and $E>E_0$, we integrate Eq. (34), written in the form

$$\partial_\gamma x=-(\cos\gamma\partial_\gamma\psi+n^{-1/2}\sin\gamma\partial_\eta\psi)e^{-\eta/\sqrt{n}}/J_0, \tag{D1}$$

$$\partial_\gamma y=(\sin\gamma\partial_\gamma\psi-n^{-1/2}\cos\gamma\partial_\eta\psi)e^{-\eta/\sqrt{n}}/J_0, \tag{D2}$$

where $\gamma=\pi/2-\theta$, and

$$\psi=\frac{h_0e^{-\beta\sqrt{\eta^2+\gamma^2}-\beta\eta}}{\sqrt{\eta^2+\gamma^2}}[\sqrt{\eta^2+\gamma^2}+\eta]^{1/2}. \tag{D3}$$

After differentiating Eq. (D3) in Eqs. (D1) and (D2), we set $\eta=0$. From the form of ψ for $\beta\gg 1$, it follows that the main contribution in Eqs. (D1) and (D2), comes from $\gamma\ll 1$. This allows us to expand $\sin\gamma$ and $\cos\gamma$ in γ, retaining only linear and quadratic terms. Then integration of Eqs. (D1) and (D2) from γ to ∞, with the boundary conditions $x(\infty)=a, y(\infty)=0$, yields

$$x=a+\frac{h_0e^{-\beta\gamma}}{J_0\sqrt{\gamma}}-\frac{h_0\sqrt{2\pi}}{J_0n^{3/4}}\operatorname{erfc}\sqrt{\beta\gamma}, \tag{D4}$$

$$y=\frac{h_0e^{-\beta\gamma}}{J_0}\left(\frac{1}{\sqrt{n\gamma}}+\sqrt{\gamma}\right)+\frac{3\sqrt{2\pi}h_0}{4J_0n^{5/4}}\operatorname{erfc}\sqrt{\beta\gamma}. \tag{D5}$$

These formulas determine parametrically the boundary $y(x)$ of the region of enhanced dissipation ($E>E_0$) around the planar defect. For $n\gg 1$, the terms proportional to the error function $\operatorname{erfc}(x)$ can be neglected, which gives Eqs. (87) and (88).

Now we calculate $\mathbf{J}(x,y)$ far away from the defect. To sum up Eq. (85), we present it in the form

$$z=-be^{i\theta}(I_0+iI_0'), \tag{D6}$$

$$I_0=\sum_{k=1}^{\infty}\frac{(-1)^k k^2}{k^2-1/4}e^{-(4k^2-1)\tau}\cos 2k\theta, \tag{D7}$$

where $I_0'=\partial_\theta I_0$, $b=4a/\pi$, and $\tau=\ln(J_c/J)>0$. We consider $\mathbf{J}(x,y)$ for $|z|\gg a$, where $J\to J_c$, thus $\tau\ll 1$. In this case I_0 reduces to

$$I_0=\sum_{k=1}^{\infty}e^{-4k^2\tau}\cos 2k\gamma+\frac{1}{4}\sum_{k=1}^{\infty}\frac{\cos 2k\gamma}{k^2-1/4}, \tag{D8}$$

where the complimentary angle $\gamma(x,y)=\pi/2-\theta$ is small (see Fig. 15). The second sum is rapidly converging, so we omitted the factor $e^{-4k^2\tau}$, inessential for $\tau\ll 1$. The first sum is calculated using Eq. (B6), and the second sum equals $2-\pi\sin\gamma$. Hence

$$I_0=\frac{\sqrt{\pi}}{4\sqrt{\tau}}e^{-\gamma^2/4\tau}-\frac{\pi}{4}\sin\gamma, \tag{D9}$$

$$I_0'=\frac{\sqrt{\pi}\gamma}{8\tau^{3/2}}e^{-\gamma^2/4\tau}+\frac{\pi}{4}\cos\gamma. \tag{D10}$$

Combining Eqs. (D6) and (D10), we obtain the following parametric description of $z(\tau,\gamma)$:

$$x=-b(\sin\gamma I_0-\cos\gamma I_0'), \tag{D11}$$

$$y=-b(\cos\gamma I_0+\sin\gamma I_0'). \tag{D12}$$

To reveal the d lines, we calculate the function $\gamma(x,y)$ from Eqs. (D11) and (D12), expressing τ for $x \gg a, y<0$ as follows:

$$\tau = -\frac{\gamma[x\sin\gamma + y\cos\gamma]}{2[x\cos\gamma - y\sin\gamma]}. \tag{D13}$$

Substituting Eq. (D13) into Eqs. (D11) and (D12), and expanding in $\gamma \ll 1$, we obtain the following relation:

$$\frac{8x^2}{\pi b^2} = \frac{(1+\gamma\xi)}{(\xi-\gamma)^3\gamma}\exp\left[-\frac{\gamma(1+\gamma\xi)}{\xi-\gamma}\right], \tag{D14}$$

which determines $\gamma(x,y)$ as a function of x and $\xi = -y/x$. Now we find the position of the d line, on which the spatial derivatives of $\gamma(x,y)$ diverge. Considering Eq. (D14) as an explicit expression of the form $x = x(\xi,\gamma)$, we conclude that $\partial_\gamma x = 0$, that is, the gradient of γ along the line $y = -\xi x$ diverges on the d line. Differentiating Eq. (D14) over γ for $\xi = \text{const}$, we obtain that the condition $\partial_\gamma x = 0$ gives $\gamma = \xi/2$. Substituting this back into Eq. (D14), we arrive at Eq. (89).

APPENDIX E: DISSIPATION

To transform from integration over $dxdy$ to the hodograph variables in Eq. (90), we write $dxdy = Wd\theta dE$, where the Jacobian, $W = \partial_\theta x \partial_E y - \partial_\theta y \partial_E x$, is calculated using Eqs. (34) and (35). This yields

$$W = \frac{1}{J^2}\left(E(\partial_E\psi)^2 + \frac{\sigma}{J}(\partial_\theta\psi)^2\right). \tag{E1}$$

The value Q does not change sign for any isotropic $J(E)$ with a positive differential conductivity, $\sigma = \partial J/\partial E$. This fact makes the hodograph transformation a single-valued procedure, that is, a given solution $\psi(E,\theta)$ corresponds uniquely to physical distributions of **E** and **J** in the coordinate space xy.

To calculate ΔQ in the flux flow region near the edge of a half infinite cut, we substitute $\psi = A\sin\theta/E$ in Eq. (91) and integrate over θ from 0 to π:

$$\Delta Q = \frac{\pi}{2}A^2\int_{E_c}^{\infty}\left(1+\frac{\sigma E}{J}\right)\frac{dE}{JE^2}. \tag{E2}$$

Integrating the second term in the brackets by parts, we obtain

$$\int_{E_c}^{\infty}\frac{\sigma dE}{J^2 E} = \frac{1}{E_c J_c} - \int_{E_c}^{\infty}\frac{dE}{JE^2}. \tag{E3}$$

After substituting Eq. (E3) into Eq. (E2), the integral terms cancel out and we arrive at Eq. (93).

To calculate Q for a planar defect, we present Eq. (94) in the form

$$Q = \frac{4E_0h_0^2}{J_0}\left(1+\frac{1}{n}\right)\sum_{m=1}^{\infty}\left(\frac{(\alpha_{2m-1}+\beta)^2}{\alpha_{2m-1}^2(\alpha_{2m-1}+\beta+1/\sqrt{n})} - \frac{(\alpha_{2m}-\beta)^2}{\alpha_{2m}^2(\alpha_{2m}-\beta-1/\sqrt{n})}\right). \tag{E4}$$

For $n \gg 1$, the terms in the brackets decay rather slowly with m, so the main contribution to the sum comes from $m \gg 1$. In this case we can neglect $1/\sqrt{n}$ in the denominators and rewrite Eq. (E4) in the form

$$Q = \frac{4E_0h_0^2}{J_0}\sum_{m=1}^{\infty}\left[\left(\frac{1}{\alpha_{2m-1}} - \frac{1}{\alpha_{2m}}\right) + \beta\left(\frac{1}{\alpha_{2m-1}^2} + \frac{1}{\alpha_{2m}^2}\right)\right], \tag{E5}$$

where $\alpha_m = \sqrt{m^2+\beta^2}$. Expanding $1/\alpha_{2m-1} \approx 1/\alpha_{2m} - 0.5\partial_m(1/\alpha_{2m})$ in the first parentheses and using Euler's formula (B6), we obtain that the sum of the first term in the square brackets equals $1/2\alpha_0 = 1/2\beta$. The summation of the second term in the square brackets yields $\pi/2 - 1/2\beta$. Combining these two contributions, we obtain

$$Q = 2\pi E_0 h_0^2/J_0 = a^2 J_0 E_0 n^{3/2}, \tag{E6}$$

where we used Eq. (63) for h_0. Equation (E6) gives the leading term in the expansion of $Q(n)$ in $n \gg 1$. In Eq. (95) we also took into account the next term of order $a^2 J_0 E_0 \sqrt{n}$, obtained from the best fit of the full dependence $Q(n)$ given by Eq. (E4). Eq. (95) not only well describes the exact $Q(n)$, but also provides the correct limit $Q = 0$ for $n = 1$.

In conclusion, we calculate Q for a planar defect in Ohmic conductors ($n = 1$). It is instructive to do so using Eq. (51), which gives the complex electric field $E\exp(-i\theta) = -dw/dz$ in the form

$$Ee^{-i\theta} = -i\frac{zE_0}{\sqrt{z^2-a^2}}. \tag{E7}$$

Substituting Eq. (E7) into Eq. (90), we obtain

$$\frac{Q}{Q_0} = \int_0^{2\pi}d\alpha\int_0^{\rho_c}\left[\frac{\rho^2}{\sqrt{\rho^4 - 2\rho^2\cos 2\alpha + 1}} - 1\right]\rho d\rho, \tag{E8}$$

where $Q_0 = \sigma E_0^2 a^2$, $x = a\rho\cos\alpha$, $y = a\rho\sin\alpha$. To avoid the formally diverging integral in the brackets, we introduce an auxiliary constant $\rho_c \gg 1$ and obtain after integration over ρ in the limit $\rho_c \to \infty$:

$$Q = Q_0\int_0^{\pi}[\cos 2\alpha\ln(2\rho_c^2/e) - \cos 2\alpha\ln(1-\cos 2\alpha) - 1]d\alpha. \tag{E9}$$

The term proportional to $\ln\rho_c$ vanishes after integration over α. Integrating the second term in Eq. (E9) by parts, we obtain that it cancels the contribution from the last term in the integrand, giving $Q = 0$. Thus a planar defect in an infinite Ohmic conductor does not cause any excess overall dissipation. In this case excess dissipation at the edges is exactly compensated by reduced dissipation in stagnation regions.

[1] G. Blatter, M.V. Feigelman, V.B. Geshkenbein, A.I. Larkin, and V.M. Vinokur, Rev. Mod. Phys. **66**, 1125 (1994).
[2] E.H. Brandt, Rep. Prog. Phys. **58**, 1465 (1995).
[3] Y. Yeshurun, A.P. Malozemoff, and A. Shaulov, Rev. Mod. Phys. **68**, 911 (1996).
[4] A. Gurevich and H. Küpfer, Phys. Rev. B **48**, 6477 (1993); A. Gurevich, Int. J. Mod. Phys. B **9**, 1054 (1995); A. Gurevich and E.H. Brandt, Phys. Rev. Lett. **73**, 178 (1994); E.H. Brandt, *ibid.* **76**, 4030 (1996).
[5] C.J. van der Beek, P.H. Kes, M.R. Maley, M.J.V. Menken, and A.A. Menovsky, Physica C **195**, 307 (1992); A.A. Zhukov, H. Küpfer, V.A. Ryabchuk, L.A. Ponomarenko, V.A. Murashov, and Yu. A. Martynkin, *ibid.* **219**, 99 (1994); M. Nideröst, A. Suter, P. Visani, A.C. Mota, and G. Blatter, Phys. Rev. B **53**, 9286 (1996).
[6] D.C. Larbalestier, Science **274**, 736 (1996); IEEE Trans. Appl. Supercond. **7**, 90 (1997).
[7] A.E. Pashitski, A. Gurevich, A.A. Polyanskii, D.C. Larbalestier, A. Goyal, E.D. Specht, D.M. Kroeger, J.A. DeLuca, and J.E. Tkaczykl, Science **275**, 367 (1997); A. Polyanskii, A. Pashitski, A. Gurevich, J.A. Parrel, M. Polak, D.C. Larbalestier, S.R. Foltyn, and P.N. Arendt, Adv. Supercond. **9**, 469 (1997).
[8] M. Polak, J.A. Parrell, A.A. Polyanskii, A.E. Pashitski, and D.C. Larbalestier, Appl. Phys. Lett. **70**, 1034 (1997); X.Y. Cai, A. Polyanskii, Q. Li, G.N. Riley, and D.C. Larbalestier, Nature (London) **392**, 906 (1998).
[9] Th. Schuster, T. Kuhn, E.H. Brandt *et al.*, Phys. Rev. B **52**, 10 375 (1995); **54**, 3514 (1996); **56**, 3413 (1997).
[10] V.K. Vlasko-Vlasov, G.W. Crabtree, U. Welp, and V.I. Nikitenko (unpublished).
[11] J.P. Clerc, G. Giraud, J.M. Laugier, and J.M. Luck, Adv. Phys. **39**, 191 (1990); M.B. Isichenko, Rev. Mod. Phys. **64**, 961 (1992).
[12] A. Gurevich and V.M. Vinokur, Phys. Rev. Lett. **83**, 3037 (1999).
[13] A. Gurevich, Fiz. Tverd. Tela (Leningrad) **30**, 1384 (1988) [Sov. Phys. Solid State **30**, 800 (1988)]; Phys. Rev. B **42**, R4857 (1990); A. Gurevich, H. Küpfer, and C. Keller, Europhys. Lett. **15**, 789 (1991).
[14] J. Straley and S. Kenkel, Phys. Rev. B **29**, 6299 (1984); E. Hinrichsen, S. Roux, and A. Hansen, Physica C **167**, 433 (1990); P.L. Leath and W. Xia, Phys. Rev. B **44**, 9619 (1991); R. Haslinger and R. Joynt, *ibid.* **61**, 4206 (2000).
[15] A. Goyal, E.D. Specht, D.M. Kroeger, and T.A. Manson, Appl. Phys. Lett. **68**, 711 (1996); E.D. Specht, A. Goyal, and D.M. Kroeger, Phys. Rev. B **53**, 3585 (1996).
[16] V.M. Vinokur, M.V. Feigelman, and V.B. Geshkenbein, Phys. Rev. Lett. **67**, 915 (1991).
[17] E.H. Brandt, Phys. Rev. B **54**, 3530 (1996); **54**, 4246 (1996); **55**, 14 513 (1997); **58**, 6506 (1998); **58**, 6523 (1998); **59**, 3369 (1999).
[18] C.P. Bean, Rev. Mod. Phys. **36**, 31 (1964).
[19] A.M. Campbell and J.E. Evetts, Adv. Phys. **21**, 1191 (1972).
[20] Th. Schuster, H. Kuhn, and M.V. Indenbom, Phys. Rev. B **52**, 15 621 (1995).
[21] A. Gurevich, Phys. Rev. B **46**, 3638 (1992).
[22] A. Gurevich and J. McDonald, Phys. Rev. Lett. **81**, 2546 (1998).
[23] S.A. Chaplygin, *On Gas Jets* (Brown University, Providence, RI, 1944); L.I. Sedov, *Two-Dimensional Problems in Hydrodynamics and Aerodynamics* (Interscience, New York, 1965).
[24] L.D. Landau and E.M. Lifshits, *Fluid Mechanics* (Pergamon, Oxford, 1987); L.M. Milne-Thompson, *Theoretical Aerodynamics* (Dover, New York, 1973).
[25] M. Friesen and A. Gurevich (unpublished).
[26] K. Seeger, *Semiconductor Physics* (Springer-Verlag, Berlin, 1982).
[27] W.T. Norris, J. Phys. D **3**, 489 (1970).
[28] J.R. Clem, R.P. Huebener, and D.E. Gallus, J. Low Temp. Phys. **12**, 449 (1973).
[29] E. Zeldov, A.I. Larkin, V.B. Geshkenbein, M. Konczykowski, D. Mayer, B. Khaykovich, V.M. Vinokur, and H. Shtrikman, Phys. Rev. Lett. **73**, 1428 (1994).
[30] E. Zeldov, J.R. Clem, M. McElfresh, and M. Darwin, Phys. Rev. B **49**, 9802 (1994).
[31] E.H. Brandt and M.V. Indenbom, Phys. Rev. B **48**, 12 893 (1994).
[32] L.D. Landau and E.M. Lifshits, *Electrodynamics of Continuous Media*, Theoretical Physics Vol. VIII (Pergamon, Oxford, 1963).
[33] I.N. Vekua, *Generalized Analytical Functions* (Pergamon, London, 1962).
[34] P.M. Morse and H. Feshbach, *Methods of Theoretical Physics* (McGraw-Hill, New York, 1953).
[35] Equations (57)–(63) were obtained for $n \gg 1$, so they do not reduce to the Ohmic case ($n=1$), described by Eqs. (51) and (52). However the discrepancy between Eqs. (57)–(63) and the exact solution becomes exponentially small for $n>3$, since the accuracy of Eqs. (57)–(63) is of order $\exp(-\pi\beta) \ll 1$. The discrepancy manifests itself as a mismatch of two exact hodograph solutions $\psi_+(x,y)$ and $\psi_-(x,y)$ at the contour $E(x,y)=E_0$, which separates the regions of current flow with $E>E_0$ and $E<E_0$, respectively. This mismatch is visible at $n<3$, but becomes undetectable in Figs. 11–16, which correspond to $n>3$.
[36] A.V. Gurevich, R.G. Mints, and A.L. Rakhmanov, *The Physics of Composite Superconductors* (Begell House, New York, 1997).
[37] *Handbook of Mathematical Functions*, Applied Mathematics Series Vol. 55, edited by M. Abramowitz and I.R. Stegun (National Bureau of Standards, Washington, DC, 1964).
[38] X.D. Wu, S.R. Foltyn, P.N. Arendt, W.R. Blumenthal, I.H. Campbell, J.D. Cotton, J.Y. Coulter, W.L. Hults, M.P. Maley, H.F. Safar, and J.L. Smith, Appl. Phys. Lett. **67**, 2397 (1995); D.P. Norton, A. Goyal, J.D. Budai, D.K. Christen, D.M. Kroeger, E.O. Specht, Q. He, B. Saffian, M. Paranthaman, C.E. Klabunde, D.F. Lee, B.C. Sales, and F.A. List, Science **274**, 755 (1996).
[39] L.N. Bulaevskii, J.R. Clem, L.I. Glazman, and A.P. Malozemoff, Phys. Rev. B **45**, 2545 (1992).